Available online at www.sciencedirect.com
ScienceDirect
Progress in Aerospace Sciences 42 (2006) 377–418
PROGRESS IN AEROSPACE SCIENCES
www.elsevier.com/locate/paerosci

Navier–Stokes analysis methods for turbulent jet flows with application to aircraft exhaust nozzles

Nicholas J. Georgiadis*, James R. DeBonis

NASA Glenn Research Center, Cleveland, OH 44135, USA

Abstract

This article presents the current status of computational fluid dynamics (CFD) methods as applied to the simulation of turbulent jet flowfields issuing from aircraft engine exhaust nozzles. For many years, Reynolds-averaged Navier–Stokes (RANS) methods have been used routinely to calculate such flows, including very complex nozzle configurations. RANS methods replace all turbulent fluid dynamic effects with a turbulence model. Such turbulence models have limitations for jets with significant three-dimensionality, compressibility, and high temperature streams. In contrast to the RANS approach, direct numerical simulation (DNS) methods calculate the entire turbulent energy spectrum by resolving all turbulent motion down to the Kolmogorov scale. Although this avoids the limitations associated with turbulence modeling, DNS methods will remain computationally impractical in the foreseeable future for all but the simplest configurations. Large-Eddy simulation (LES) methods, which directly calculate the large-scale turbulent structures and reserve modeling only for the smallest scales, have been pursued in recent years and may offer the best prospects for improving the fidelity of turbulent jet flow simulations. A related approach is the group of hybrid RANS/LES methods, where RANS is used to model the small-scale turbulence in wall boundary layers and LES is utilized in regions dominated by the large-scale jet mixing. The advantages, limitations, and applicability of each approach are discussed and recommendations for further research are presented.

Keywords: Jet; Turbulence; Nozzle; LES; RANS

Contents

*Corresponding author. Tel.: +1 216 433 3958; fax: +1 216 977 7500.
E-mail address: Georgiadis@nasa.gov (N.J. Georgiadis).

0376-0421/$ - see front matter © 2007 Elsevier Ltd. All rights reserved.
doi:10.1016/j.paerosci.2006.12.001

1. Introduction

Computational fluid dynamics (CFD) is routinely used for the analysis of aerospace systems due to advances in flow solver and computer hardware technologies. For the investigation of one particular class of flows, that of aircraft engine exhaust nozzles, Reynolds-averaged Navier–Stokes (RANS) solvers have been used extensively in recent years and have been successful in calculating performance quantities such as thrust. With regulations on aircraft noise becoming increasingly more stringent throughout the world, reduction of the noise produced from the exhaust system, jet noise, has become a major focus of the aerospace industry. To be able to contribute to jet noise reduction efforts, CFD methods must be able to accurately calculate the turbulent fluid structures that produce jet noise. Despite significant work to improve RANS-based methods, in which all effects of turbulence are replaced by a turbulence model, these methods have limitations for jets with significant three-dimensionality, compressibility, and high temperature streams. In addition, RANS methods by definition can only provide time-averaged turbulent information. As a result, the CFD community has begun investigating methods that directly compute the turbulence that causes jet noise, such as large eddy

Nomenclature

a	speed of sound
C_P	specific heat at constant pressure
D	jet diameter
D_P	primary nozzle diameter for dual stream jets
D_S	secondary nozzle diameter for dual stream jets
e_t	total energy
G	filter function
k	turbulent kinetic energy
k_t	turbulent thermal conductivity
L_t	turbulent length scale
M_a	acoustic Mach number
M_t	turbulent Mach number
P	static pressure
P_T	stagnation pressure
Pr_t	turbulent Prandtl number
$\mathscr{P}$	turbulent production
q_j	heat flux
q_j^{sgs}	subgrid scale heat flux
q_j^T	turbulent heat flux
r	distance to centerline
R	correlation coefficient
Re_t	turbulent Reynolds number
S_{ij}	rate of strain tensor
t	time
t^*	characteristic time
T	static temperature
T_r	static temperature ratio
T_t	stagnation temperature
T_g	stagnation temperature gradient
t	time
U_C	convection velocity
U_{jet}	jet exit velocity
U_P	primary jet exit velocity for dual stream jets
u	velocity
u'	fluctuating velocity
W_{ij}	vorticity tensor
x, y, z	Cartesian coordinates
y^+	wall normal coordinate
χ	vortex stretching invariant
Δ	filter width
ε	turbulent dissipation rate
ε_s	solenoidal turbulent dissipation rate
κ	Von Karman constant
μ_t	dynamic eddy viscosity
μ_T	total eddy viscosity, Tam–Ganesan model
μ_ρ	density contribution to the eddy viscosity
ν	kinematic viscosity
ν_t	kinematic eddy viscosity
ω	specific turbulent dissipation rate
ω_{ij}	normalized rotation tensor
Ω	vorticity magnitude
ρ	density
τ	turbulent time scale
τ_{ij}	viscous stress tensor
τ_{ij}^{sgs}	subgrid scale stress tensor
τ_{ij}^T	turbulent stress tensor

simulation (LES) techniques. This article provides an overview of the calculation methods that are being applied to turbulent jet flows. While the primary goal of improving these methods is to enable better prediction of jet aeroacoustics, the focus here is addressing capabilities to compute the underlying turbulent jet fluid dynamics.

We begin by identifying some of the nozzle concepts that have been the focus of recent jet noise reduction research to illustrate the types of problems that CFD is needed to compute. One nozzle concept that is currently entering service on commercial airliners is the chevron nozzle (Fig. 1). The serrated edge of the chevron nozzle increases the mixing of the exhaust streams and modifies the turbulent characteristics in the jet, reducing noise [1]. There are several other noise reduction concepts currently being studied. Most concepts, such as plasma actuators [2], fluidic injection [3], tabs [4,5] and lobed mixers [6] (Fig. 2) aim to increase mixing and modify the jet turbulence similar to the chevron nozzle. Papamoschou has developed a series of nozzles that are referred to as offset fan flow technology concepts [7–12]. The objective is to divert the fan flow below the core stream and change the noise directivity and intensity. Implementation of the offset fan flow idea would be through devices such as vanes or wedges (Fig. 3).

Design and analysis of these concepts can be greatly enhanced through the use of CFD. CFD has been successfully used for years for the development of other aerospace components. To date almost all

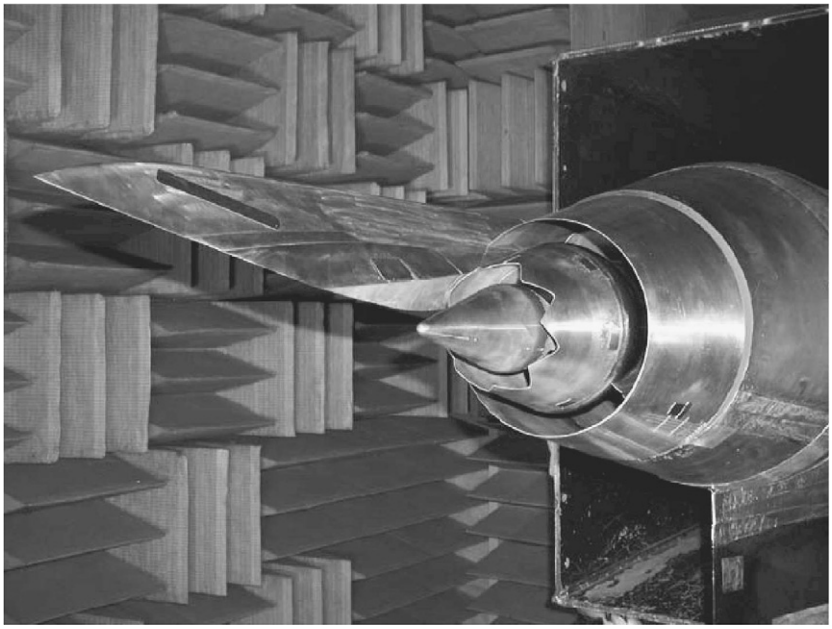

Fig. 1. Chevron nozzle with pylon, installed in the NASA Langley Low Speed Aeroacoustic Wind Tunnel (from [116]).

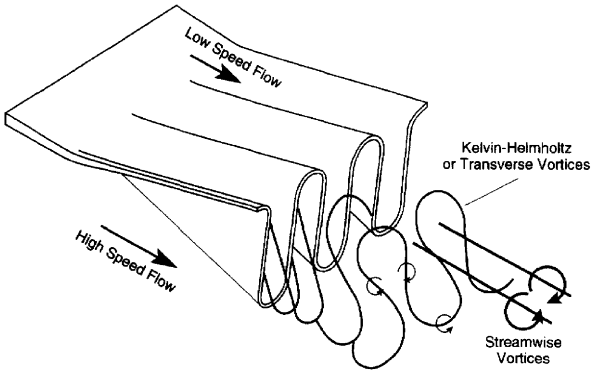

Fig. 2. Schematic of a lobed mixer (from [6]).

CFD for design and development has been steady RANS calculations. However, RANS turbulence models have been found to have a number of limitations for jet flows [13]. A significant amount of work has been done in the area of advanced RANS models specifically for jets [14–16]. The results have been mixed, and generalizing these models to a wide range of flow conditions and geometries may not be possible. RANS is also limited in the information it can provide. For most jet applications a linear two-equation $k-\varepsilon$ or $k-\omega$ model is typically used [17]. In recent years, non-linear explicit algebraic stress model (EASM) formulations have been explored for improving the capability to predict turbulent jet flow fields with significant turbulent anisotropy [18–21]. However, EASMs utilize an underlying two-equation approach and are subject to the same deficiencies as the linear two-equation models. All RANS models can only provide a simple statistical representation of the turbulence in the form of the turbulent kinetic energy and a local length scale.

Acoustic predictions based on RANS solutions are performed using the acoustic analogy [22,23]. This acoustic modeling relies heavily on constructing the acoustic source from the RANS solutions [24]. The results from this method are reasonable for cold round jets. Results are poor for heated jets and non-axisymmetric geometries.

While direct numerical simulation (DNS) hopefully one day will enable accurate calculations of turbulent jets without need for modeling any of the turbulent spectrum, LES is now the next logical step towards improved jet predictions. Over the last decade LES has been increasingly used due to the growth in computing power. LES is an unsteady method which directly computes the large-scale turbulent structures and reserves modeling for the small-scale turbulence. The direct simulation of large-scale structures can significantly enhance our understanding of the flow and lead to better noise reduction strategies and improved designs.

The LES of the jet near field captures the non-linear sound generation process. It is possible but

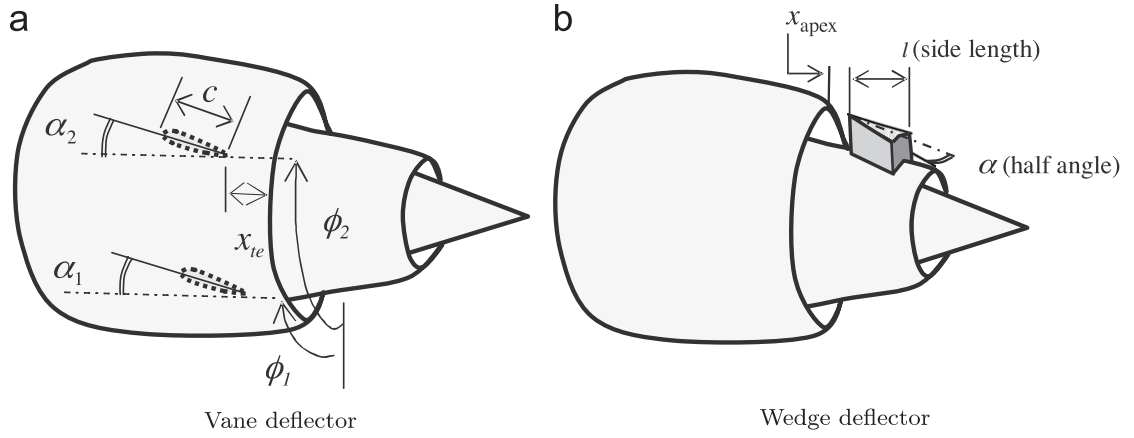

Fig. 3. Offset fan flow nozzle concepts (from [12]). (a) Vane deflector. (b) Wedge deflector.

not efficient to carry the simulation to the acoustic farfield to compute the noise directly. The propagation of the sound to the farfield is a linear process and can instead be predicted by several simpler methods. Shih et al. [25] gives a good discussion and evaluation of these methods. LES has the potential to vastly improve the prediction of jet flows and impact designs of noise suppressing nozzles. However, there is much work that needs to be done before LES can be used reliably in this manner.

This article is divided between RANS modeling and unsteady modeling methods, wherein the latter, LES is emphasized. In the RANS modeling section, details of widely used general purpose RANS turbulence models and some recently developed jet-specific turbulence models are presented. Several benchmark jet cases are investigated using these turbulence models to illustrate the capabilities of these RANS turbulence models. The unsteady modeling section begins with a description of the DNS and LES approaches. Recent examples of LES as applied to jet flows are provided next. Finally, key issues in LES that are either areas of current research or areas of needed work are addressed.

2. RANS modeling

While RANS methods are used routinely for analysis of aerospace systems, the accurate prediction of nozzle and jet flows remains an area of needed improvement. Turbulence modeling remains the pacing item limiting the accuracy of jet flow predictions. For aeroacoustics analysis, both the mean flow and turbulence state are important for assessment of noise emitted by jets under consideration. RANS techniques will be required for the foreseeable future, especially for the analysis of complex nozzle geometries. As a result, there is a need for a comprehensive assessment of RANS modeling capabilities and limitations.

One standard form of the continuity, momentum, and energy equations is as follows:

$$\frac{\partial \overline{\rho}}{\partial t} + \frac{\partial}{\partial x_i}(\overline{\rho}\hat{u}_i) = 0, \tag{1}$$

$$\frac{\partial}{\partial t}(\overline{\rho}\hat{u}_i) + \frac{\partial}{\partial x_j}(\overline{\rho}\hat{u}_i\hat{u}_j) + \frac{\partial \overline{P}}{\partial x_i} - \frac{\partial \overline{\tau}_{ij}}{\partial x_j} - \frac{\partial \tau_{ij}^{\mathrm{T}}}{\partial x_j} = 0, \tag{2}$$

$$\frac{\partial}{\partial t}(\overline{\rho}\hat{e}_t) + \frac{\partial}{\partial x_j}(\overline{\rho}\hat{u}_j\hat{e}_t + \hat{u}_j\overline{P}) - \frac{\partial}{\partial x_j}(\hat{u}_i\overline{\tau}_{ij} + \hat{u}_i\tau_{ij}^{\mathrm{T}}) + \frac{\partial}{\partial x_j}(\overline{q}_j + q_j^{\mathrm{T}}) = 0. \tag{3}$$

Eqs. (1)–(3) are obtained utilizing mass-weighted Reynolds averaging as given by

$$\hat{u}_i = \frac{1}{\overline{\rho}\tau}\int_t^{t+\tau} \rho u_i \, \mathrm{d}t. \tag{4}$$

The unclosed terms from the RANS momentum and energy equations are the Reynolds stress shown in Eq. (2) and the turbulent heat flux, which is given in Eq. (3). In linear eddy viscosity models, the Boussinesq approximation is used to relate the turbulent Reynolds stress to the mean rate of strain tensor through a turbulent (or eddy) viscosity:

$$\tau_{ij}^{\mathrm{T}} = -\mu_t\left(2\hat{S}_{ij} - \tfrac{2}{3}\frac{\partial \hat{u}_k}{\partial x_k}\delta_{ij}\right). \tag{5}$$

The rate of strain is tensor, $\hat{S}_{ij}$, is given by

$$\hat{S}_{ij} = \frac{1}{2}\left(\frac{\partial \hat{u}_j}{\partial x_i} + \frac{\partial \hat{u}_i}{\partial x_j}\right). \quad (6)$$

Similarly, the turbulent heat flux is related to the temperature gradient through a turbulent conductivity, k_t:

$$q_j^T = -k_t \frac{\partial \hat{T}}{\partial x_j}. \quad (7)$$

The turbulent Prandtl number, Pr_t is used to relate the turbulent viscosity to the turbulent conductivity:

$$Pr_t = \frac{\mu_t C_P}{k_t}. \quad (8)$$

Using Eq. (8) and assuming a constant turbulent Prandtl number, the turbulent heat flux is expressed as a function of the turbulent viscosity that is used to calculate the Reynolds stress. While many production CFD codes suggest a default setting for $Pr_t = 0.9$, some authors such as Birch [26,27] have suggested that $Pr_t = 0.7$ is more appropriate for jet flows. Birch further suggests a zonal approach where $Pr_t = 0.4$ is used through the potential core of the jet and then $Pr_t = 0.7$ is used beyond the end of the potential core. There have recently been models under development to take into account variations in the turbulent Prandtl number such as the work of Kenzakowski et al. [28,29].

Within the class of RANS methods, two-equation turbulence models have been used most frequently for jet aeroacoustics analyses because of their capability to provide mean flow and turbulent kinetic energy fields necessary for subsequent acoustic analysis. EASM formulations have also been considered recently. They have not resulted in significant improvements to jet flow predictions over linear two-equation models. There have been several investigations of turbulence models for jet flows originating from a variety of nozzle configurations such as those in Refs. [18–21,30,31]. A comprehensive review of turbulence model development in the PAB3D code and evaluation for a variety of nozzle flows is presented in Abdol-Hamid et al. [32] While the majority of jet flow simulations to date have been conducted using structured grids, some recent efforts such as that of Pao et al. [33] have investigated unstructured grids.

Capturing the initial jet growth region remains a difficulty for RANS models with the calculated jet mixing rates generally being much lower than that exhibited by experimental data. For example, Koch et al. [30] investigated subsonic axisymmetric separate flow jets with three flow solvers using two-equation $k-\varepsilon$ turbulence models where the mixing rate in each of the calculations was lower than that indicated by experimental results. The turbulent kinetic energy levels were also lower, which corresponds to the slower mixing rate. Engblom et al. [31] investigated a series of cold and hot single flow subsonic nozzle flows including a baseline round nozzle and several chevron nozzles, and a similar trend in the computations indicated much lower spreading towards the nozzle centerline than observed in experiments. Georgiadis et al. [21] investigated a reference subsonic lobed nozzle flow with linear two-equation and explicit algebraic stress turbulence models, and found similar trends. Additionally, far downstream of the end of the jet potential core, it is generally the case that the computed farfield mixing rate becomes too high. As a result, current RANS turbulence models are not adequate for accurate prediction of jet flow details.

There have been recent efforts to improve the accuracy of two-equation models as applied to jet flows. Thies and Tam [34] proposed a $k-\varepsilon$ model with different closure coefficients compared with standard $k-\varepsilon$ models. These modified closure coefficients were recalibrated using a series of jet flows. To account for the effects of compressibility, the correction due to Sarkar [35,36] was employed. Additionally, the round jet correction of Pope [37] is used implicitly with the Tam–Thies model. Tam and Ganesan [38] extended the work of Thies and Tam by incorporating a correction for heated jets. Abdol-Hamid et al. [39] also proposed a correction to enable more accurate prediction of heated jets using a $k-\varepsilon$ model with standard closure coefficients. Massey et al. [40] demonstrated the improved capability of this corrected model in the PAB3D code to calculate heated jets, including those from complex installed engine configurations with nozzles employing chevrons. Engblom et al. [41] developed a $k-\varepsilon$ correction to be coupled with a standard $k-\varepsilon$ model in order to accurately predict the rapid turbulent mixing exhibited by experimental results that is not modeled by standard two-equation models. This correction modifies the coefficients in the diffusion terms of both the k and ε equations to enable more rapid diffusion of these turbulent quantities when the ratio of the turbulent length

scale to the distance from the centerline becomes large.

In this article, we first compare the capabilities of these newer turbulence modeling approaches with existing standard two-equation models for a benchmark jet test case free of any compressibility or three-dimensionality effects. Data from experiments performed on a round nozzle operating at unheated and heated low subsonic conditions are used to avoid modeling complexities associated with compressible jet mixing. Mean axial velocities and turbulent kinetic energy in the developing jet flowfields are used to conduct the turbulence model evaluations. In latter parts of this RANS section, the effects of compressibility, three-dimensionality, and multiple-stream jets are investigated utilizing well established reference nozzle experiments.

2.1. Linear two-equation turbulence modeling details

The Wind RANS solver was used for all of the turbulence model investigations described in the RANS section of this paper, with one similar solver, CFL3D, also being employed in the lobed nozzle discussion. In Refs. [21,42], Wind was found to provide nearly identical results to those obtained from other production CFD solvers for jet flows when the same turbulence model was employed. As a result, it is expected that the results obtained here with Wind are representative of those that would be obtained from other CFD solvers. Two of the turbulence models investigated here fall into the class of standard models as they do not have any model specifics tuned for jet flows and are already available as part of the production code version of Wind. These models are the Chien $k-\varepsilon$ [43] formulation and the Menter shear stress transport [44,45] (SST) formulation which uses a $k-\omega$ model in near wall regions and a standard $k-\varepsilon$ model transformed to a $k-\omega$ set for regions away from walls such as in jet mixing regions. The other three modeling approaches were implemented as part of this work. First, the total temperature correction of Abdol-Hamid et al. [39] demonstrated in the PAB3D code [40] was built upon the Chien $k-\varepsilon$ model in Wind, and will be referred to as the PAB temperature correction or PAB TC. The second model is the $k-\varepsilon$ model due to Tam–Ganesan [38] which as discussed previously, incorporates a density based correction added to the original Tam–Thies [34] formulation. Third, the variable diffusion model was also built upon the Chien $k-\varepsilon$ model in Wind. Details of the equation sets for all of the turbulence models and associated corrections are provided in the remainder of this section.

2.1.1. Chien model

The Chien $k-\varepsilon$ model solves an equation set that for regions away from walls, i.e. in jet regions, is nearly identical to that of the Jones–Launder model [46] which is considered the standard $k-\varepsilon$ model [17]. The k and ε equations are as shown in Eqs. (9) and (10). Note that the near wall terms, which have no effect in the jet region, are not shown here to enable the most straightforward comparison with the other models described in this section:

$$\frac{D(\rho k)}{Dt} = \tau_{ij}\frac{\partial u_i}{\partial x_j} - \rho\varepsilon + \frac{\partial}{\partial x_j}\left[\left(\mu + \frac{\mu_t}{\sigma_k}\right)\frac{\partial k}{\partial x_j}\right], \tag{9}$$

$$\frac{D(\rho\varepsilon)}{Dt} = C_{\varepsilon 1}\frac{\varepsilon}{k}\tau_{ij}\frac{\partial u_i}{\partial x_j} - C_{\varepsilon 2}\frac{\varepsilon^2}{k} + \frac{\partial}{\partial x_j}\left[\left(\mu + \frac{\mu_t}{\sigma_\varepsilon}\right)\frac{\partial \varepsilon}{\partial x_j}\right]. \tag{10}$$

The eddy viscosity is calculated as

$$\mu_t = C_\mu \rho \frac{k^2}{\varepsilon}. \tag{11}$$

The Chien model closure coefficients are $C_\mu = 0.09$, $\sigma_k = 1.0$, $\sigma_\varepsilon = 1.3$, $C_{\varepsilon 1} = 1.35$, and $C_{\varepsilon 2} = 1.80$. In jet regions, the Jones–Launder model differs from the Chien model only in that $C_{\varepsilon 1} = 1.44$, and $C_{\varepsilon 2} = 1.92$. Turbulent heat flux is calculated using the eddy viscosity expression shown in Eq. (11) and the turbulent Prandtl number is set to $Pr_t = 0.7$. This setting for Pr_t was used for all of the turbulence models described in this section, with the exception of the Tam–Ganesan model which prescribes $Pr_t = 0.422$. In Refs. [47,48], it was found that variation of Pr_t had substantial effect on computed temperature fields, but minimal effect on mean velocity and turbulent kinetic energy fields, which are the quantities examined in this section.

2.1.2. Menter SST model

The Menter SST model is a two-layer model which employs the original $k-\omega$ model of Wilcox [49] in the inner region of boundary layers (with modification of turbulent diffusion coefficients) and switches to a $k-\varepsilon$ model in the outer region of boundary layers and in mixing regions. The outer $k-\varepsilon$ model is transformed to provide a second set of

$k-\omega$ equations with a blending function used to transition between the two sets of equations. The SST model has been found to provide very good calculations of wall bounded flows even with large separation regions. One example of this may be found in Ref. [50] where the SST model was found to provide the best predictions of several one- and two-equation models in the Wind code for separated nozzle flows. The details of the complete SST model are provided in Refs. [44,45], but here we only consider the outer equation set, which is in effect for jet calculations. In particular, we consider the differences between the model and the exact transformation of the standard $k-\varepsilon$ model shown in Eqs. (9)–(11).

The specific dissipation rate, ω is defined as

$$\omega = \frac{\varepsilon}{\beta^* k}, \tag{12}$$

with $\beta^* = C_\mu = 0.09$. The $k-\omega$ set of equations employed in jet regions is

$$\frac{D(\rho k)}{Dt} = \tau_{ij}\frac{\partial u_i}{\partial x_j} - \beta^*\rho\omega k + \frac{\partial}{\partial x_j}\left[(\mu + \sigma_{k2}\mu_t)\frac{\partial k}{\partial x_j}\right], \tag{13}$$

$$\frac{D(\rho\omega)}{Dt} = \gamma\frac{\omega}{k}\tau_{ij}\frac{\partial u_i}{\partial x_j} - \beta_2\rho\omega^2 + \frac{\partial}{\partial x_j}\left[(\mu + \sigma_{\omega2}\mu_t)\frac{\partial \omega}{\partial x_j}\right] + 2\rho\sigma_{\omega2}\frac{1}{\omega}\frac{\partial k}{\partial x_j}\frac{\partial \omega}{\partial x_j}, \tag{14}$$

where $\beta_2 = 0.0828$, $\gamma = 0.44$, $\sigma_{k2} = 1.0$, and $\sigma_{\omega2} = 0.857$. The turbulent viscosity is then calculated as

$$\mu_t = \rho\frac{a_1 k}{\max(a_1\omega, \Omega)}, \tag{15}$$

where $a_1 = 0.31$ and Ω is the vorticity magnitude. Eq. (15) is identical to Eq. (11) for $\Omega < a_1\omega$. Some of the subscripts in Eqs. (12) and (14) have a 2 in reference to this equation set being the outer formulation, while the inner model, not shown here, have a 1 in the subscripts. The k-equation (Eq. (13)) does transform exactly from that of the standard $k-\varepsilon$ model (Eq. (9)), but the transformation of the standard ε-equation (Eq. (10)) to an equation for ω results in an expression that differs from Eq. (14) as shown next:

$$\frac{D(\rho\omega)}{Dt} = \gamma\frac{\omega}{k}\tau_{ij}\frac{\partial u_i}{\partial x_j} - \beta_2\rho\omega^2 + \frac{\partial}{\partial x_j}\left[(\mu + \sigma_{\omega2}\mu_t)\frac{\partial \omega}{\partial x_j}\right] + 2\rho\sigma_{\omega2}\frac{1}{\omega}\frac{\partial k}{\partial x_j}\frac{\partial \omega}{\partial x_j} + \underline{\frac{\omega}{k}\frac{\partial}{\partial x_j}\left[(\sigma_{\omega2} - \sigma_{k2})\mu_t\frac{\partial k}{\partial x_j}\right]}. \tag{16}$$

The underlined term in Eq. (16) is an extra diffusion term resulting from the exact transformation of Eq. (10) that is not included in Eq. (14) of the SST model. The production term of the SST model, as suggested in Ref. [51], usually employs the rotation tensor instead of the rate-of-strain tensor. In addition, the ω-equation diffusion coefficient transforms from the ε equation as $\sigma_{\omega2} = 1/\sigma_\varepsilon = 1/1.3 = 0.769$. In Ref. [51], $\sigma_{\omega2} = 0.857$, which corresponds to $\sigma_\varepsilon = 1.17$. This value is used to enable better agreement for the logarithmic portion of boundary layers. The value assigned to the coefficient in the production of dissipation, $\gamma = 0.44$, results from satisfying the equation:

$$\gamma = \beta_2/\beta^* - \sigma_{\omega2}\kappa^2/\sqrt{\beta^*} \tag{17}$$

with the von Karman constant, $\kappa = 0.41$.

2.1.3. PAB temperature correction

In Ref. [39], the temperature corrected turbulence model that we refer to as the PAB TC was built upon the Jones–Launder $k-\varepsilon$ model. As mentioned previously, the Chien $k-\varepsilon$ model is nearly identical to the Jones–Launder formulation for jet regions. As a result, for the work described here we built the PAB TC upon the Chien model in Wind. The same equations for k and ε as shown in Eqs. (9) and (10) with corresponding closure coefficients are used here. The correction modifies the coefficient, C_μ, in Eq. (11) for jet flows with a stagnation temperature gradient. The normalized stagnation temperature gradient is defined as

$$T_g = \frac{|\nabla T_t|}{T_t}(k^{3/2}/\varepsilon). \tag{18}$$

The coefficient C_μ then becomes a function of this stagnation temperature gradient:

$$C_\mu = 0.09\left[1 + \frac{T_g^3}{0.041 + f(M_t)}\right], \tag{19}$$

where

$$f(M_t) = (M_t^2 - M_{t0}^2)H(M_t - M_{t0}) \tag{20}$$

and the turbulent Mach number is defined as

$$M_t = \sqrt{2k}/a. \tag{21}$$

In Eq. (20), M_{t0} is set to 0.1. For very sharp stagnation temperature gradients, C_μ can become very large, and in Ref. [40], C_μ was capped to not exceed 5 times the standard value of 0.09 and this same restriction was used for the calculations discussed in this article. Finally, the PAB TC also employs the Sarkar compressibility correction in order to extend the model to high speed jets. The Sarkar compressibility correction modifies the dissipation rate term in the k-equation (see Eq. (9)) via the expression:

$$\varepsilon = \varepsilon_s(1 + \alpha M_t^2), \tag{22}$$

where ε_s is the solenoidal dissipation rate solved via Eq. (10). The coefficient, α, is set to the default value of 1.0.

2.1.4. Tam–Thies and Tam–Ganesan models

As mentioned previously, the Tam–Ganesan model extended the previous model developed by Tam and Thies to improve predictions for heated jets. The original Tam–Thies model solved a $k-\varepsilon$ equation set as follows:

$$\frac{D(\rho k)}{Dt} = \tau_{ij}\frac{\partial u_i}{\partial x_j} - \rho\varepsilon + \frac{\partial}{\partial x_j}\left[\left(\mu + \frac{\mu_t}{\sigma_k}\right)\frac{\partial k}{\partial x_j}\right], \tag{23}$$

$$\frac{D(\rho\varepsilon_s)}{Dt} = C_{\varepsilon 1}\frac{\varepsilon_s}{k}\tau_{ij}\frac{\partial u_i}{\partial x_j} - (C_{\varepsilon 2} - C_{\varepsilon 3}\chi)\frac{\varepsilon_s^2}{k} + \frac{\partial}{\partial x_j}\left[\left(\mu + \frac{\mu_t}{\sigma_\varepsilon}\right)\frac{\partial \varepsilon_s}{\partial x_j}\right], \tag{24}$$

where the vortex stretching term is given by

$$\chi = \omega_{ij}\omega_{jk}S_{ki}. \tag{25}$$

The normalized rotation and rate-of-strain tensors are given by

$$\omega_{ij} = \frac{1}{2}\frac{k}{\varepsilon_s}\left(\frac{\partial u_i}{\partial x_j} - \frac{\partial u_j}{\partial x_i}\right), \tag{26}$$

$$S_{ij} = \frac{1}{2}\frac{k}{\varepsilon_s}\left(\frac{\partial u_i}{\partial x_j} + \frac{\partial u_j}{\partial x_i}\right). \tag{27}$$

The turbulent viscosity is given as

$$\mu_t = C_\mu \rho \frac{k^2}{\varepsilon_s}. \tag{28}$$

The Sarkar compressibility correction as given by Eq. (22) is used with the coefficient $\alpha = 0.518$. The other closure coefficients are $C_\mu = 0.0874$, $\sigma_k = 0.324$, $\sigma_\varepsilon = 0.377$, $C_{\varepsilon 1} = 1.40$, and $C_{\varepsilon 2} = 2.02$. The coefficient multiplying the vortex stretching term in Eq. (25), $C_{\varepsilon 3}$, is set to 0.822. Most notably, the diffusion coefficients σ_k and σ_ε are significantly smaller than those used for the standard $k-\varepsilon$ model and since they appear in the denominator of the diffusion terms of Eqs. (23) and (24), these settings result in more diffusion of k and ε than that with the standard model. Tam and Thies set Pr_t to 0.422.

Tam and Ganesan [38] used instability theory to show that for a heated jet, where the density of the jet is less than the ambient, turbulent mixing should be greater than for an unheated jet. They proposed a modification to the Tam–Thies model where the total turbulent viscosity is given by

$$\mu_T = \mu_t + \mu_\rho \tag{29}$$

and the density contribution to the total turbulent viscosity is given by

$$\mu_\rho = \begin{cases} C_\rho \dfrac{k^{7/2}|(\nabla\rho)\cdot(\nabla u)|}{\varepsilon^2 \quad |(\nabla u)|}, & (\nabla\rho)\cdot(\nabla u) < 0, \\ 0, & (\nabla\rho)\cdot(\nabla u) > 0, \end{cases} \tag{30}$$

where the closure coefficient $C_\rho = 0.035$.

2.1.5. Variable diffusion model

A correction to the Chien $k-\varepsilon$ model was proposed in Ref. [41] to account for the deficiency in standard two-equation models to reproduce the experimentally observed enhanced mixing near the end of the jet potential core. This enhanced mixing was hypothesized to be due to increased shear layer instability via acoustic interaction near the end of the potential core. It was proposed that as the size of the largest turbulent eddies became close to the width of the potential core, acoustic radiation across the potential core would lead to increased fluid dynamic instability and greater turbulent mixing. The correction proposed that this increased mixing be modeled via greater turbulent diffusion when the potential core width (characterized by the distance to the centerline) was similar to that of the turbulent length scale,

$$L_t = C_D\frac{k^{3/2}}{\varepsilon}. \tag{31}$$

In Eq. (31), $C_D = 0.164$. The turbulent diffusion coefficients are modified according to

$$\sigma_{k(\text{modified})} = \sigma_k \frac{(1 + AF)}{(1 + AF/\beta)}, \tag{32}$$

$$\sigma_{\varepsilon(\text{modified})} = \sigma_\varepsilon \frac{(1 + AF)}{(1 + AF/\beta)}, \tag{33}$$

where AF is the acoustic factor that compares distance to the centerline, r, with the turbulent length scale:

$$AF = \left(C_e \frac{k^{3/2}/\varepsilon}{r} \right)^3 \tag{34}$$

with $\beta = 0.25$ and $C_e = 0.5$. With $\beta = 0.25$, Eqs. (32) and (33) show that the diffusion coefficients will become 4 times smaller than the standard values when the turbulent length scale becomes very large in comparison to the potential core width, and will result in increased turbulent diffusion in such regions.

2.2. Incompressible round jets

Two test points from the NASA Glenn Research Center's Acoustic Reference Nozzle (ARN) database [52] were investigated for the turbulence models described in the previous section. All of the jets from the ARN experiments issued from a 2 in. (5.08 cm) diameter convergent nozzle. The two test points each had a jet acoustic Mach number, M_a (defined as the jet exit velocity normalized by the ambient speed of sound) = 0.5, which indicates that compressibility effects would not be an important factor for the jets under consideration. One of these two test points, corresponding to Setpoint 3 from the ARN database, used unheated laboratory air while the second, corresponding to Setpoint 23, had the jet supply stream heated such that the static temperature ratio, T_r, (defined as the static temperature of the jet at the nozzle exit plane normalized by the ambient static temperature) was equal to 1.76. In the ARN experiments, extensive measurements of mean velocities and turbulent statistics were made using particle image velocimetry (PIV), which are used here for comparison to the RANS computations. For the unheated case, several sets of data were available with some scatter in the results. The data set used here for comparisons with the computations was selected because mean axial velocities and axial turbulence intensities agreed closely with the hot-wire measurements for a similar round jet experiment from Ref. [53].

All of the simulations discussed in this article utilized structured grids. For the incompressible round jets discussed in this section, a three-zone axisymmetric computational grid was generated with grids packed to nozzle wall surfaces such that the first point off of the wall would correspond to an average $y+$ of approximately 1. Fig. 4 shows the computational grid near the nozzle exit. This same grid packing strategy was used for all of the other nozzle cases discussed in the RANS portion of this article. The jet plume zone extended 40 nozzle diameters, $40D$, in the axial direction and $25D$ radially from the nozzle jet centerline.

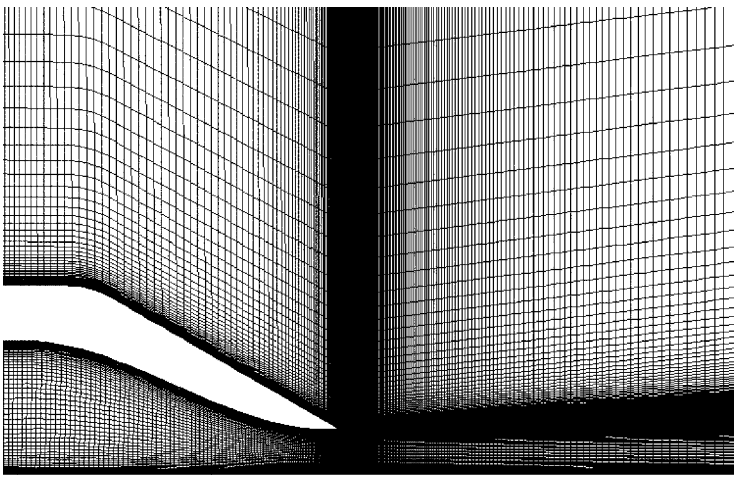

Fig. 4. Computational grid for incompressible jet calculations.

The stagnation temperature and pressure were specified as boundary conditions at the nozzle entrance. For the unheated case, the nozzle stagnation pressure was set to 1.197 times the freestream static pressure and the stagnation temperature was set equal to the freestream static temperature. For the heated case, the nozzle stagnation pressure was set to 1.103 times the freestream static pressure and the stagnation temperature was set equal to 1.815 times the freestream static temperature. For both cases, the stagnation pressure and temperature set at the inflow of the freestream zone were set to the freestream static values to model the ambient conditions surrounding the jet.

2.2.1. Incompressible cold round jets

A comparison of centerline axial velocities obtained from the five turbulence modeling approaches is made with experimental data for the unheated case in Fig. 5. Note that in these figures for the unheated case, we refer to the Tam–Thies model, which provides identical results to that of the Tam–Ganesan extension in the absence of a temperature or density gradient in the jet mixing layer. Fig. 5 shows that the SST model produces the longest potential core due to inhibited initial turbulent growth rate. Beyond the potential core, however, the rate of jet decay is faster than that produced by the other models and the experimental

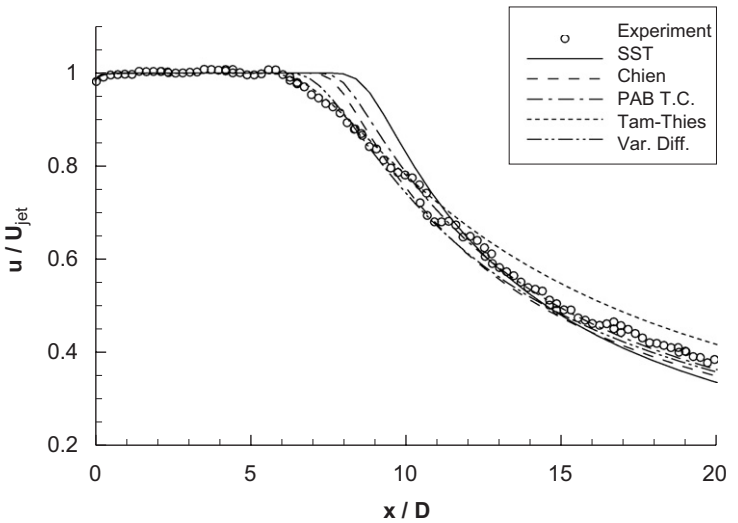

Fig. 5. Centerline axial velocity profiles for unheated jet.

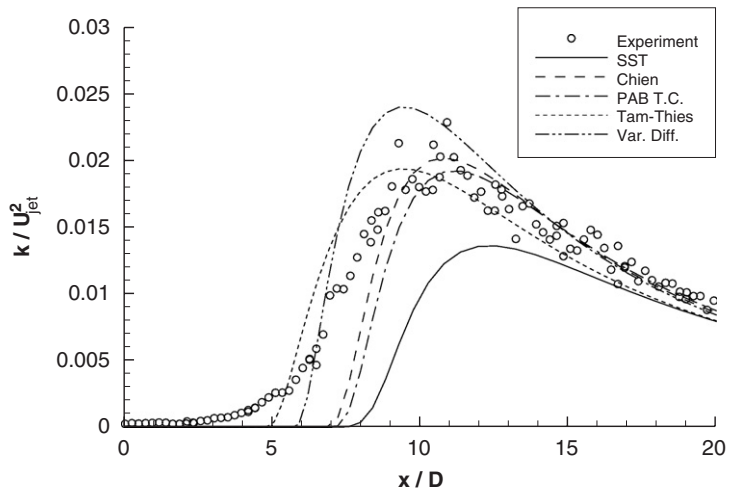

Fig. 6. Centerline turbulent kinetic energy profiles for unheated jet.

data. The Chien k–ε and PAB TC. k–ε models also produce potential core lengths that are too long, and then downstream mixing rates that are too high relative to the experimental data. These results are characteristic of standard two-equation models. For this unheated case, the PAB TC results cannot be expected to provide better agreement than a standard k–ε model such as Chien. The PAB TC results have a slightly longer potential core than the Chien results because the Sarkar correction is used implicitly with the PAB TC formulation. Even for this jet flow case with minimal compressibility, the Sarkar correction makes a difference because it is formulated to use the ratio of the turbulent kinetic energy to the local speed of sound squared as shown in Eq. (21).

The Tam–Thies model and the variable diffusion (var. diff.) model results show better agreement with experimental data in terms of the potential core lengths. For both of these models, the improved agreement is due to a much higher turbulent diffusion relative to the other models. Downstream of the potential core, the rate of decay in centerline velocity is lowest for the Tam–Thies model, which is

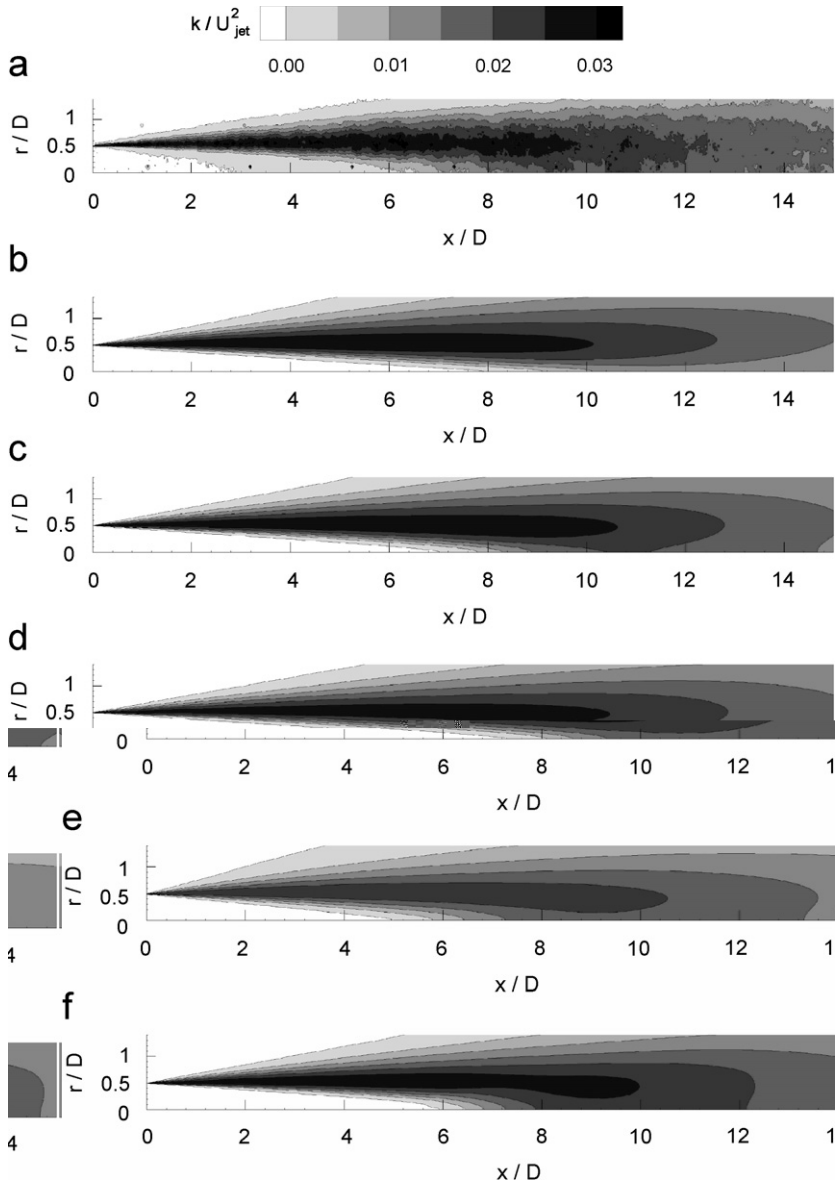

Fig. 7. Turbulent kinetic energy contours for unheated jet: (a) experiment; (b) SST; (c) Chien; (d) PAB TC; (e) Tam–Thies; (f) Var. diff.

primarily due to the use of the vortex stretching correction.

The calculated turbulent kinetic energy along the jet centerline is compared with experimental data in Fig. 6 and the models exhibit substantial scatter. The SST results show the slowest propagation of turbulence to the jet centerline. It is important to note that although the SST model uses a transformed $k-\varepsilon$ model in free shear layer regions such as this jet mixing region, the resulting $k-\omega$ equations and closure coefficients were established to provide optimal results for wall boundary layers, and are not identical to those obtained from an exact transformation of the standard $k-\varepsilon$ equations as discussed previously. The var. diff. and Tam–Thies approaches enable a faster transport of turbulent kinetic energy to the centerline than the turbulence models employing standard diffusion coefficients. This is more readily observed in the turbulent kinetic energy contours shown in Fig. 7. For the Tam–Thies model, the turbulent diffusion coefficients are set to smaller constant values leading to higher diffusion everywhere. The var. diff. model only changes the diffusion coefficients from the standard values when the ratio of the turbulent length scale to the distance from the jet centerline is large. The PIV data indicate a strongly diffused shear layer at the end of the potential core. Both the Tam–Thies and var. diff. $k-\varepsilon$ solutions again produce much more rapid diffusion of turbulence to the centerline. The peak turbulent kinetic energy produced in the jet shear layer by the Tam–Thies model is lower than that of the other solutions and the experimental data.

2.2.2. *Incompressible heated round jets*

The heated case is examined next. A comparison of centerline axial velocities obtained from all of the turbulence modeling approaches is made with experimental data in Fig. 8. In order to determine the effect of the Tam–Ganesan correction to the original Tam–Thies model, we present both sets of results in this section. The two standard models, SST and Chien $k-\varepsilon$, again produce the longest potential core lengths. The Tam–Thies and Tam–Ganesan models start off with potential cores that are slightly longer than the experimental data, but the farfield decay rate is lower than that of the other models. As for the unheated case, the vortex stretching term produces this lower farfield jet decay rate. The Tam–Ganesan model indicates slightly more mixing than that of the Tam–Thies model. For a similar heated case in Ref. [11], a larger variation was noted between results obtained with the two model formulations. The differences with the results obtained here may be due to the upstream modeling. In Ref. [11], the jet calculations were initiated at the nozzle exit, while in the calculations discussed here, the upstream nozzle was modeled with a calculated turbulent boundary layer provided by the Chien $k-\varepsilon$ model.

The PAB TC provides the best agreement with experimental data in terms of the potential core length and mean velocities as shown in Fig. 7. Recalling that for the unheated case, the Chien k–ε

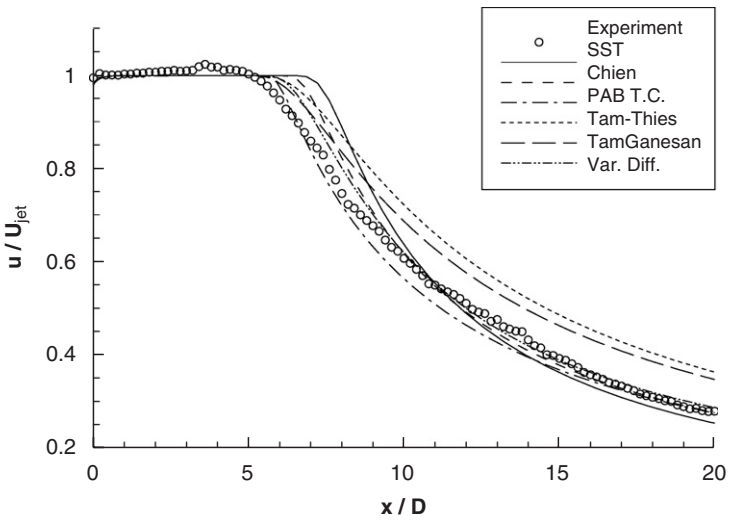

Fig. 8. Centerline axial velocity profiles for heated jet.

and PAB TC model results were very similar, the PAB TC results shown here indicate that its temperature correction produces the correct trend in faster mixing due to jet heating. The var. diff. model, despite having no modification specific to heated jets, also provides generally good agreement with the experimentally measured velocities. While this model worked well for the round jets under consideration here, the model would be difficult to generalize for jets in which a jet centerline could not be easily determined or for multiple jets.

Examining the experimental data for the centerline turbulent kinetic energy for the heated case in Fig. 9 and for the unheated case in Fig. 6, it is interesting to note that the experiment indicates some turbulence at the jet centerline just downstream of the nozzle exit, even before any significant jet mixing occurs. It is hypothesized that a large fraction of what is experimentally measured as turbulence just downstream of the nozzle exit (near $x/D = 0$), may be fluctuations in the potential flow due to turbulence in the jet shear layer away from the centerline. The nature of the RANS calculations prohibits fluctuations in the inviscid core of the jet to be calculated. The turbulence models can only produce and sustain turbulence in the presence of mean velocity shear, which is absent in this region.

The turbulent kinetic energy along the centerline shown in Fig. 9 indicates similar trends to those observed for the unheated case. In particular, the models employing modifications to the standard diffusion coefficients (Tam–Thies, Tam–Ganesan, and var. diff.) enable the fastest transport of turbulent kinetic energy to the centerline and best agreement with experimental data. For this heated case, the PAB TC solution mixes more quickly than the standard Chien k–ε model solution (which is the underlying model with no temperature correction). However, the turbulent kinetic energy contours in Fig. 10 indicate that the turbulent kinetic energy produced by the PAB TC has a smaller peak region and dissipates more quickly than the standard model and experimental data. The PAB TC achieves more rapid mixing in the mean flow due to a modification to the eddy viscosity expression and not to the turbulent kinetic energy equation. While the mean flow mixes out more quickly using the temperature correction, the balance of k, ε, and the modified μ_t actually results in the turbulent kinetic energy field dissipating too far upstream. This would likely lead to degraded results in acoustic analogy predictions using these results.

The Tam–Ganesan solution produces a slightly higher peak in turbulent kinetic energy than for the Tam–Thies model, but the peak levels are still significantly lower than the experimental data. Although not shown here, the peak turbulent viscosities obtained with the Tam–Ganesan model were approximately 15% higher than that with no density correction (Tam–Thies). The var. diff. model appears to be able to reproduce the rapid diffusion of turbulence near the end of the potential core that was found in the experiment and peak levels of turbulent kinetic energy that are in reasonable agreement with experimental data. Away from the centerline, the standard models provide turbulent kinetic energy fields that are in as

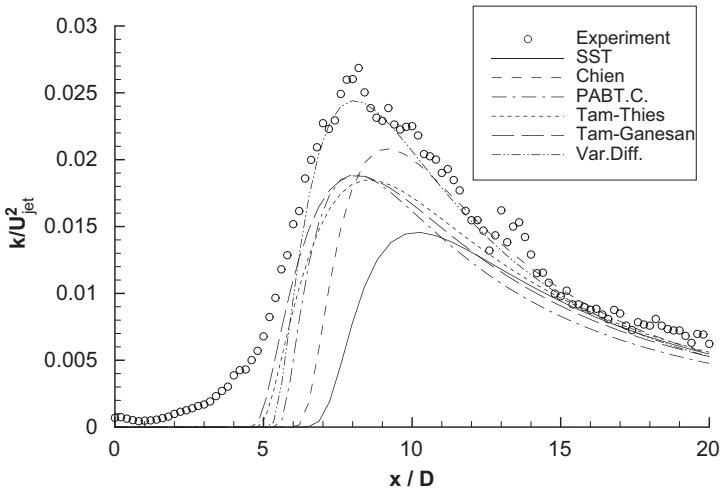

Fig. 9. Centerline turbulent kinetic energy profiles for heated jet.

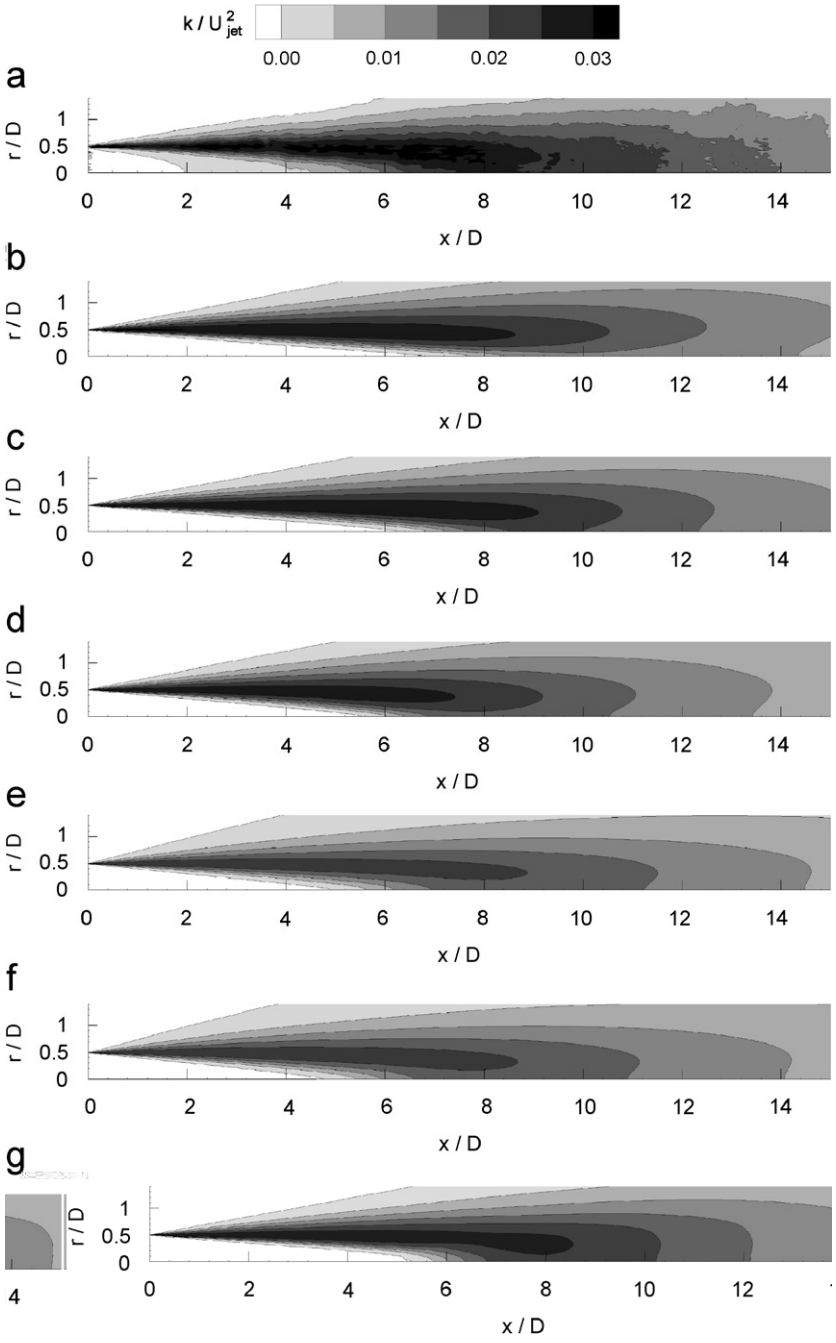

Fig. 10. Turbulent kinetic energy contours for heated jet: (a) experiment; (b) SST; (c) Chien; (d) PAB TC; (e) Tam–Thies; (f) Tam–Ganesan; (e) Var. diff.

good agreement with experimental data as any of the modified formulations.

While the modified two-equation models discussed in this section have exhibited some improvements over the standard models (i.e. SST and Chien $k-\varepsilon$ formulations), none will likely result in a broad replacement of the standard models for application to realistic nozzle and jet flows. This is because none of the new formulations are able to achieve the difficult task of being amenable to generalization to flows beyond the round jets addressed here and also being able to provide improvements to both the

mean flow and turbulent fields. In the other examples discussed in the RANS portion of this article, we concentrate on examination of the standard models. Non-linear EASMs are also investigated alongside the standard models for a lobed nozzle and coflowing nozzle.

2.3. Compressible round jets

In the previous section, round jets at nearly incompressible operating conditions were investigated. In this section, the effects of compressibility are addressed. The present study uses the benchmark experiments performed at the NASA Langley Research Center (LaRC) Jet Noise Laboratory by Seiner [54]. These experiments investigated an axisymmetric water-cooled Mach 2 nozzle with an exit diameter, $D = 3.60$ in. (91.44 mm). The nozzle operated at fully expanded conditions for this series of cases. The turbulence models utilized here were the Menter SST [44,45] and Chien $k-\varepsilon$ [43] formulations. In addition, the Chien model was used with and without the Sarkar compressibility correction [35,36], shown previously in Eq. (22). The default setting for $\alpha = 1.0$ was utilized. As discussed previously, the Sarkar compressibility correction increases the rate of turbulent kinetic energy dissipation and then lowers the resultant turbulent viscosity.

The computational model used for these calculations is analogous to that used for the incompressible axisymmetric jets described previously. The computational grid used for these calculations was a modified version of that used for the calculations discussed in Ref. [55]. The jet plume zone extended $25D$ in the axial direction and $11.1D$ radially from the jet centerline.

In Dembowski and Georgiadis [47] a comparison of computations to experiments were made for all of the operating points, with variation in jet stagnation temperature that were measured in the experiments of Ref. [54]. Results are presented here for the cold jet case ($T_r = 0.59$) in Fig. 11 and for one of the heated cases with $T_r = 2.11$ in Fig. 12. The stagnation temperature is not shown for the cold jet case. For each operating point, the Chien $k-\varepsilon$ solution obtained with no compressibility correction predicts the fastest mixing, and much faster than indicated by the experimental data. The SST solutions also consistently predict a faster mixing rate than the data. Compared with the baseline Chien model solutions, the SST results predict a

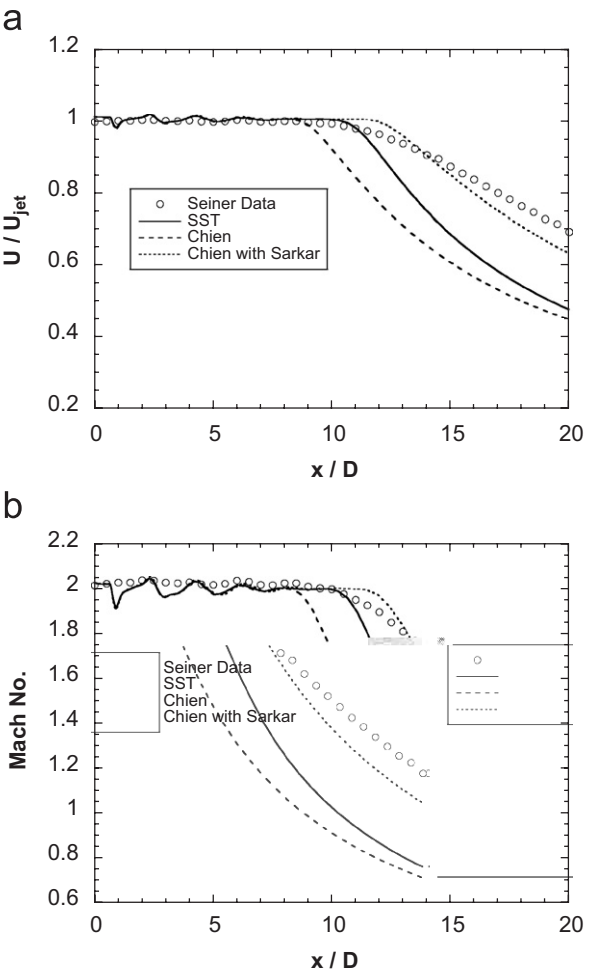

Fig. 11. Comparison of solutions for unheated Mach 2 jet. (a) Centerline axial velocity. (b) Centerline Mach number.

longer potential core, but then a steeper slope in jet decay further downstream. Recall that for the incompressible jet cases described previously, the calculated potential core lengths exceeded that of the experimental measurements although the trend of the SST results in comparison to the Chien $k-\varepsilon$ results are the same for potential core length and farfield jet decay.

The Chien model results obtained with the Sarkar compressibility correction indicate the longest potential cores and slowest mixing of any of the solutions for all of the temperatures investigated. In all cases, these solutions obtained with the compressibility correction overpredict the potential core length. Further downstream, the rate of decay is still slightly overpredicted for the unheated nozzle case, but this trend reverses for the higher temperatures.

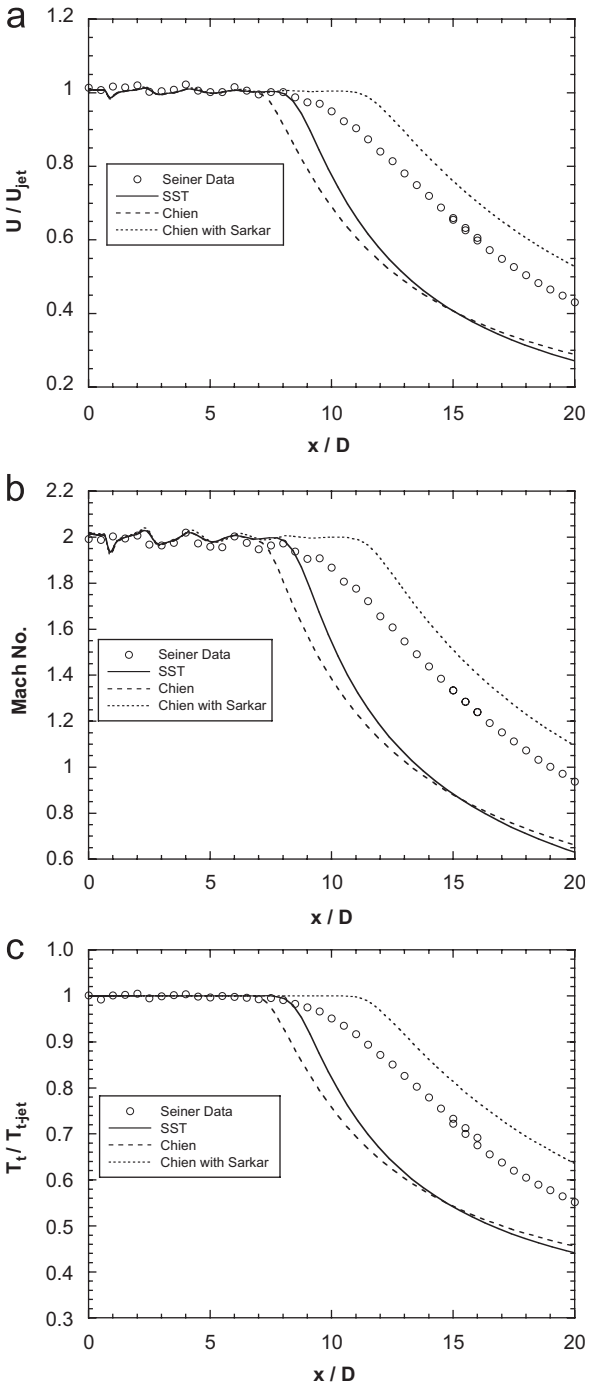

Fig. 12. Comparison of solutions for heated Mach 2 jet. (a) Centerline axial velocity. (b) Centerline Mach number. (c) Centerline stagnation temperature.

2.4. Lobed nozzles

To address the complexities of three-dimensional nozzle flowfield development, an unheated subsonic nozzle having a six-lobed configuration was investigated. Temperature and compressibility effects are not significant factors, and the effects of three-dimensional flow could be isolated.

In recent years, non-linear EASM formulations have been explored for improving the capability to predict the aerodynamics and aeroacoustics of turbulent jets [18,19,56,57]. To date, these studies have indicated that EASM approaches have difficulties similar to linear two-equation models in underpredicting initial jet mixing rates. However, it has been noted that calibrations of key EASM coefficients have not been extensively performed for free shear layer flows. EASM approaches have the potential to be more accurate than linear two-equation models when applied to flows with significant turbulent anisotropy. Two general purpose RANS solvers, CFL3D and Wind, were used to obtain calculations for this lobed nozzle configuration. Linear one- and two-equation turbulence models, as well as EASM formulations, are used here.

2.4.1. Lobed nozzle configuration

In the experiments of Zaman et al. [53], the free jets developing from a circular nozzle and three-lobed nozzles, having six, 10, and 14 lobes, respectively, were investigated. These lobed nozzle configurations exhibited lower turbulence intensities and lower far field noise than non-lobed configurations. The six-lobed configuration, shown schematically in Fig. 13, is under investigation here. All of the nozzles investigated in Ref. [53] had convergent interiors with a 0.25 in (6.35 mm) long constant area cross-section just upstream of the nozzle exit plane, which produces a jet with initially only an axial velocity component.

The equivalent diameter, D, based on an area-equivalent round nozzle, was 0.58 in. (14.73 mm) for all of the nozzles. In the experiments, hot-wire anemometry was used to make measurements of mean flow axial velocity and turbulence intensity along the centerline for unheated Mach 0.94 nozzle exit operating points. A more detailed comparison of results for both Mach 0.30 and 0.94 operating points is presented in Ref. [21].

Two widely used RANS solvers, Wind [58] and CFL3D [59], were employed to conduct the computational investigations of the six-lobed nozzle. The intent in using two distinct flow solvers was to determine if the same turbulence model installed in the two codes would yield similar results and as a

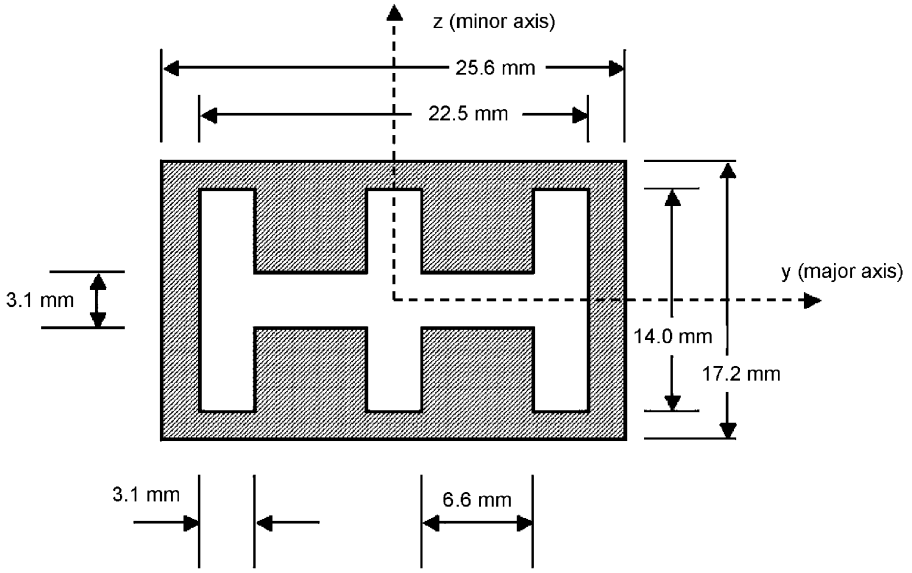

Fig. 13. Schematic of nozzle exit for six-lobed configuration.

result, if turbulence modeling effects would dominate other code numerics. A three-dimensional computational grid with approximately 2.57 million points distributed across six zones was constructed for the RANS simulations. Grid regions near nozzle surfaces were packed analogously to that described previously for the round jet simulations. The jet plume zone extended approximately $50D$ in the axial direction and $25D$ in the other two directions from the jet centerline. Boundary conditions were set in the same manner as those for the round jet cases discussed previously. That is, stagnation pressures and temperatures were applied at the nozzle inflow to achieve the desired nozzle exit Mach number, and static conditions were applied in the ambient to simulate a quiescent environment surrounding the jet.

2.4.2. Turbulence modeling

Both CFL3D and Wind have a broad set of turbulence models available, all of which fall into the class of eddy-viscosity formulations. In the current study, a subset of these models was chosen to investigate the effects of model formulations and sophistication, i.e. linear one-equation, linear two-equation, and non-linear two-equation EASM approaches. In the cases where the same model from this subset was available in both CFL3D and Wind, solutions with both codes were obtained to isolate any differences due to code numerics.

The linear one-equation model investigated with both solvers is the Spalart–Allmaras [60,61] (SA) formulation. The SA model solves a transport equation for the turbulent viscosity. Because it does not directly solve for turbulent kinetic energy nor a second quantity from which a turbulent length scale may be derived (as is done in two-equation models), SA is not frequently used for jet aeroacoustic calculations. Further, as discussed in Refs. [60,61], the SA model was tuned for wake flows at the expense of jet applications. The linear two-equation turbulence models investigated here are the Chien k–ε and Menter SST models. The Chien k–ε model is available in Wind and the SST model is available in both CFL3D and WIND.

Two non-linear EASM formulations available in the CFL3D code were utilized here. The first EASM is derived in a k–ε form [62,63] and the second is derived in a k–ω form [63]. Unlike linear two-equation models, EASM formulations account for turbulent stress anisotropies and are directly related to the full Reynolds stress model. As a result, EASM models have the capability to include more relevant flow physics than the linear models. However, they are solved using a two-equation approach and as a result are not significantly more computationally expensive than linear two-equation models. The k–ω EASM formulation in CFL3D was used in the current study. The k–ε EASM model of Rumsey et al. [62,63] is available in WIND, as

detailed in Ref. [57], and was also investigated in this study.

During the course of the current nozzle calculations, two coefficients controlling the diffusion terms in the underlying two-equation model of the k–ω EASM installed in CFL3D were modified. As a result, the principal equations defining this model are provided in the following discussion. The turbulent stress tensor of the EASM (for both k–ε and k–ω) is

$$\tau_{ij} = \tfrac{2}{3}k\delta_{ij} - 2\nu_t^*\{S_{ij} - \tfrac{1}{3}S_{kk}\delta_{ij} + [a_2a_4(S_{ik}W_{kj} - W_{ik}S_{kj}) - 2a_3a_4(S_{ik}S_{kj} - \tfrac{1}{3}S_{kl}S_{lk}\delta_{ij})]\}, \tag{35}$$

where S_{ij} is

$$S_{ij} = \frac{1}{2}\left(\frac{\partial u_i}{\partial x_j} + \frac{\partial u_j}{\partial x_i}\right), \tag{36}$$

and W_{ij} is

$$W_{ij} = \frac{1}{2}\left(\frac{\partial u_i}{\partial x_j} - \frac{\partial u_j}{\partial x_i}\right). \tag{37}$$

The kinematic eddy viscosity, ν_t^* is

$$\nu_t^* = C_\mu^* k\tau = -k\alpha_1, \tag{38}$$

where the turbulent time scale is $\tau = 1/\omega = k/\varepsilon$. The quantity α_1/τ is equivalent to $-C_\mu^*$ and is obtained from the solution to a cubic equation at every point in the flow field. The solution procedure is described in detail in Ref. [63].

The form of the k–ω model used in CFL3D as the underlying two-equation model for the EASM is

$$\frac{Dk}{Dt} = \mathscr{P} - f_{\beta^*}k\omega + \frac{\partial}{\partial x_k}\left[\left(\nu + \frac{\nu_t^*}{\sigma_k}\right)\frac{\partial k}{\partial x_k}\right], \tag{39}$$

$$\frac{D\omega}{Dt} = \gamma\frac{\omega}{k}\mathscr{P} - \beta\omega^2 + \frac{\partial}{\partial x_k}\left[\left(\nu + \frac{\nu_t^*}{\sigma_\omega}\right)\frac{\partial \omega}{\partial x_k}\right], \tag{40}$$

where the production of k is given by

$$\mathscr{P} = -\tau_{ij}\frac{\partial u_i}{\partial x_j} \approx 2\nu_t^* S_{ij}S_{ij}. \tag{41}$$

The form of the function f_{β^*} is given in Ref. [63]. Two coefficients in the k–ω EASM were modified, σ_k and γ. In the original model, $\sigma_k = 2$ and $\gamma = 0.575$. The modified coefficients are $\sigma_k = 1$ and $\gamma = 0.53$. The motivation for this change was that in the original model, the dissipation was too low near boundary layer and shear layer edges, which frequently resulted in abrupt slope changes in predicted mean-flow quantities. The problem was particularly evident for jet flows, as shown in Ref. [64]. In addition, the rate of jet mixing was found to be too low relative to experimental measurements. Reducing σ_k improved results near the edge of the jet considerably. It also improved the slope characteristics near the edge of boundary layers. In Ref. [65], a similar change to σ_k in a linear k–ε model (σ_k changed from 1.36 to 1.0) also resulted in greater mixing and better agreement with experimental observations.

The γ coefficient multiplies the production term in the ω equation, and it also affects the value of σ_ω, through the equation:

$$\sigma_\omega = \kappa^2/[\sqrt{c_\mu}(\beta - \gamma)], \tag{42}$$

where $\kappa = 0.41$, $\beta = 0.83$, and $c_\mu = 0.0895$.

Use of Eq. (42) insures correct log-layer characteristics. In the original model, $\gamma = 0.575$ results in $\sigma_\omega = 2.2035$. In the revised model, $\gamma = 0.53$ corresponds to $\sigma_\omega = 1.8730$.

The k–ω EASM with the modified coefficients was subsequently tested for a variety of validation aerodynamic flowfields, including: flat plate, back step, transonic diffuser, axisymmetric bump, airfoils, wing, ejector nozzle, and curved duct. These tests were generally very successful and were documented in Ref. [64]. Due to the general success with the modified coefficients, both for the current nozzle case as well as for the validation flows, the default k–ω EASM model in CFL3D was permanently changed, incorporating the modified coefficients. The original and new sets of coefficients are compared in the current study for the Mach 0.94 nozzle case. While the Mach 0.94 case is not a highly compressible flow, the experimental quantities appearing in the subsequent mean velocity and turbulence intensity plots are actually $\overline{(\rho u)}/\overline{(\rho u)}_{\text{jet}}$ and $(\rho u)'_{\text{rms}}/\overline{(\rho u)}_{\text{jet}}$, respectively.

Mean axial velocities and turbulence intensities from the solutions are compared with the experimental data of Zaman et al. [53]. The axial turbulence intensities were obtained from $\tau_{11} = \overline{u'u'}$ and employed the appropriate turbulent stress expression for each model as follows. From the EASM solutions, the turbulent stress tensor given by Eq. (35) was used. For the linear one-equation and two-equation model solutions, the Boussinesq approximation was employed:

$$\tau_{ij} = \tfrac{2}{3}k\delta_{ij} - 2\nu_t(S_{ij} - \tfrac{1}{3}S_{kk}\delta_{ij}). \tag{43}$$

While the two-equation models directly provide the turbulent kinetic energy k used in Eq. (43), this quantity must be approximated for the one-equation

SA model. In Ref. [61], this approximation for k is given by

$$k = \nu_t \sqrt{2S_{ij}S_{ij}}/2a_1, \tag{44}$$

where $a_1 = 0.155$ is the structure parameter.

Comparisons of centerline axial velocities obtained within each class of turbulence model are presented in Fig. 14. Centerline turbulence intensities are provided in Fig. 15. The CFL3D and Wind implementations of the same models (SA and SST) produced very similar predictions. It may be observed that the SA results indicate a shorter potential core length than the SST or Chien k–ε results. The SA solutions provide the worst agreement with the experimental data in terms of the turbulence intensity results, particularly in the farfield. This is due to the fact that the SA model does not directly solve for the turbulent kinetic energy, unlike the other models employed in this study, and the derived turbulent kinetic energy is a function of the strain rate tensor as calculated by Eq. (44). The result of the SA approximation is that as the velocity profile becomes relatively flat, the calculated turbulence intensity becomes too small. In considering only the mean axial velocity predictions, it may be concluded that the SA model performed as well as any of the models investigated here. However, the deficiency in the SA model farfield turbulence intensity would be undesirable if calculation of the turbulence intensity field is important, as in the case of a jet noise calculation employing the results of RANS flowfield computations [24,31,66].

Two k–ω EASM solutions were obtained, the first using the original settings for σ_k and γ and the second using the new settings. As shown in Fig. 14(c), the k–ω EASM solution using the new coefficients provided the highest level of mixing and closest agreement with experimental data. In Fig. 15, none of the solutions accurately capture the presence of the first turbulence intensity peak, but the k–ω EASM (new) solution indicates smaller discrepancies in prediction of the initial rise in turbulence intensity than the other two EASM solutions. Interestingly, the CFL3D k–ω EASM solution with the original coefficient settings and the WIND k–ε EASM solution produce similar results.

2.5. Multiple stream jets

On modern commercial aircraft, the most commonly used jet engine is the separate-flow turbofan, with coaxial primary and bypass exhaust streams.

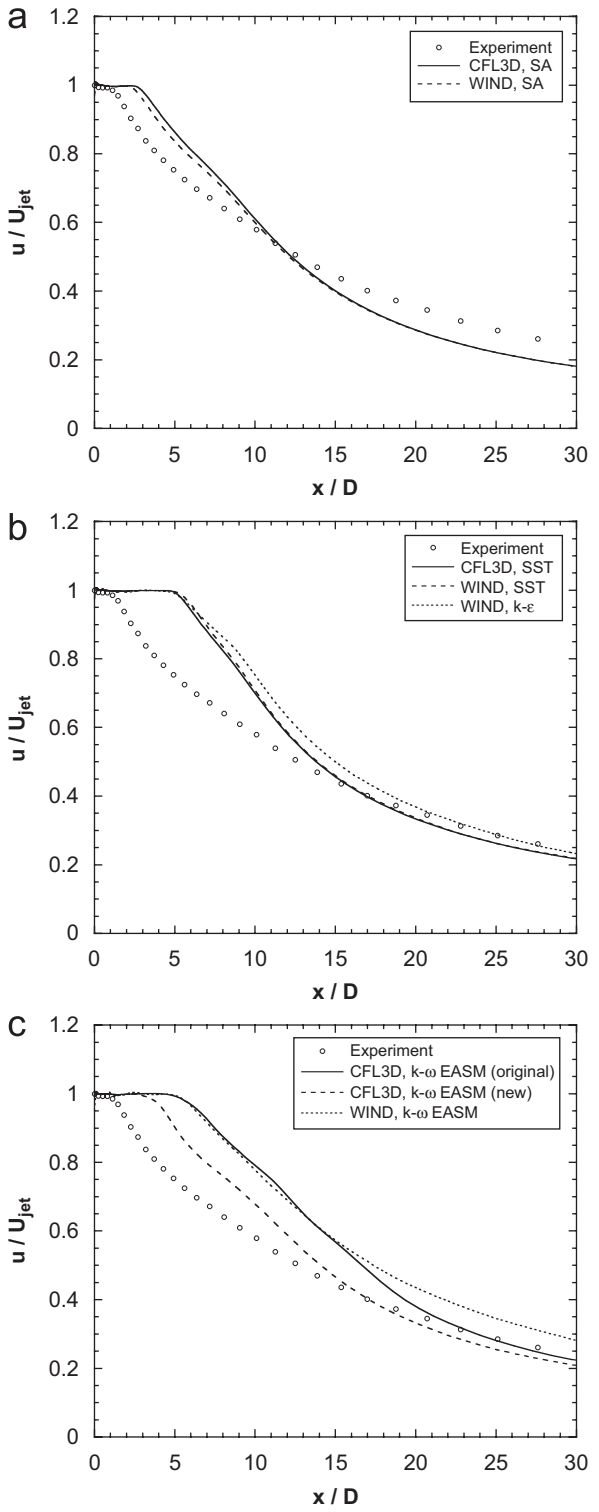

Fig. 14. Mean velocities along the centerline for the Mach 0.94 lobed nozzle. (a) One-equation models. (b) Two-equation models. (c) Explicit algebraic stress models.

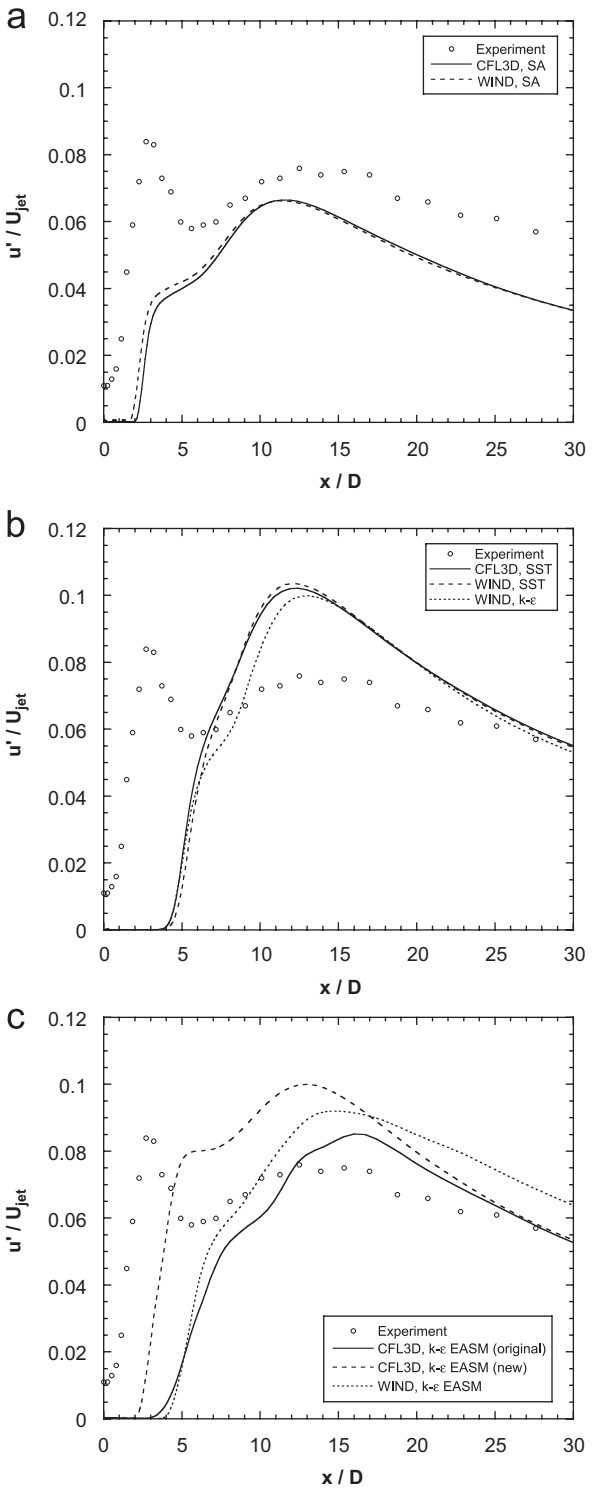

Fig. 15. Turbulence intensities along the centerline for the Mach 0.94 lobed nozzle. (a) One-equation models. (b) Two-equation models. (c) Explicit algebraic stress models.

At first impression, it may be anticipated that the noise produced by the primary jet in such coaxial configurations could be reduced by a shielding effect due to the secondary (bypass) flow. In Refs. [8,9], however, it was shown that the primary jet potential core in coaxial arrangements is actually lengthened, while the secondary stream becomes mixed out well upstream of the end of the primary stream potential core. As a result, a significant portion of the core noise is still emitted by the primary jet stream.

In recent years, a series of experimental investigations on multiple stream jets at the University of California, Irvine (UCI) has investigated alternatives to the coaxial arrangement [7–12]. These include eccentric nozzle configurations, in which the primary (inner) nozzle is translated vertically up to the bypass (upper) nozzle surface. More recently, exhaust nozzle configurations which use vanes installed near the exhaust plane in the bypass duct to deflect the bypass stream have also been investigated. Both of these configurations have been shown to produce significant reduction in noise relative to a coaxial nozzle geometry. In both modified configurations, the noise reduction is accomplished due to a shortening of the primary flow potential core, and an increase in the amount of secondary flow on the underside of the nozzle.

2.5.1. Coaxial nozzle investigations

The focus of the calculations considered initially, and described here, is the more traditional coaxial arrangements, for which the UCI experimental studies have provided an extensive set of velocity profiles for a parametric variation in secondary (bypass) nozzle area and secondary flow Mach number [8]. Comparisons of the RANS calculations were made with the UCI experimental data to determine if the RANS calculations can capture the experimentally observed jet flow development as a function of the secondary flow area and Mach number.

The coaxial nozzle arrangements employed a fixed inner (primary) nozzle and a variety of outer (secondary) nozzles. Air at room temperature was supplied to the primary and secondary nozzles. The primary nozzle had an exit diameter $D_P = 12.7$ mm and lip thickness of 0.4 mm, and was designed by the method of characteristics for Mach number $M_P = 1.5$. The Reynolds number of the primary jet was 550,000. Three conical secondary nozzles were used, with exit diameters $D_S = 17.8, 21.6,$ and 25.4 mm. Fig. 16 depicts the nozzle configuration

for the coaxial arrangement with $D_S = 17.8$ mm. The primary jet was perfectly expanded and the surrounding air was at ambient, still conditions. The secondary flow was naturally pressure-matched at subsonic conditions. Nozzle configurations and flow conditions are summarized in Tables 1 and 2. For ease of reference, a labeling system that describes the size and shape of the secondary nozzle and the Mach number of the secondary flow is used. Coaxial nozzles are denoted by *Cxx* where $xx = 10D_S/D_P$. The secondary flow is denoted by *Myy*, where $yy = 100M_S$. Case C20M37, for example, describes the coaxial jet with Mach 0.37 secondary flow exhausting from a coaxial arrangement with $D_S/D_P = 2.0$. The single Mach 1.5 jet is denoted single.

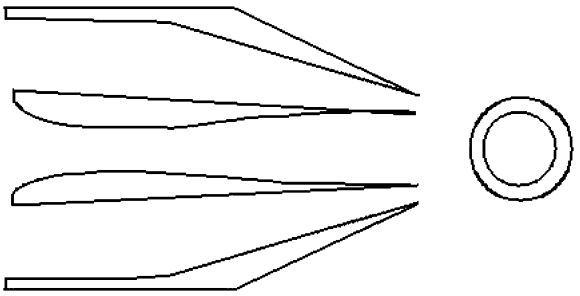

Fig. 16. Schematic of coaxial nozzle arrangement.

Table 1
Nozzle geometry

Nozzle	D_s/D_p	A_s/A_p
C14	1.4	0.9
C17	1.7	1.8
C20	2.0	2.9

Table 2
Unheated primary jet flow conditions

Case	M_P	U_P (m/s)	ρ_P/ρ_∞	M_S	U_s (m/s)	ρ_S/ρ_∞
Single	1.5	430	1.45	0	0	1.00
M37	1.5	430	1.45	0.37	130	1.03
M60	1.5	430	1.45	0.60	210	1.07
M90	1.5	430	1.45	0.90	290	1.16

Computational grids for the single and coaxial nozzles were constructed as follows. Since all of the calculations discussed here were run using Wind in axisymmetric mode, two-dimensional grids were employed. For the single jet nozzle, a three zone grid was constructed and for each of the three coaxial nozzle configurations listed in Table 1, a four zone grid was constructed. Fig. 17 shows details of the axisymmetric grid for the C20 coaxial nozzle near the nozzle exit plane. For all of the single and coaxial nozzle cases investigated here, the grids extended 60 D_P downstream of the nozzle exit and 24 D_P vertically from the axis of symmetry. The grids were packed to nozzle surfaces for proper application of the turbulence models in the near wall boundary layer regions.

Initial calculations were obtained with the Menter SST, Chien k–ε, and Rumsey k–ε EASM turbulence models. In each of these calculations, it was noted that the turbulent boundary layers developing inside the primary nozzle resulted in a slightly underexpanded flow condition at the nozzle exit, where the calculated exit plane Mach number, approximately 1.45 for each of these cases, was lower than the design exit Mach number = 1.5. This was the result of the turbulent boundary layer displacement

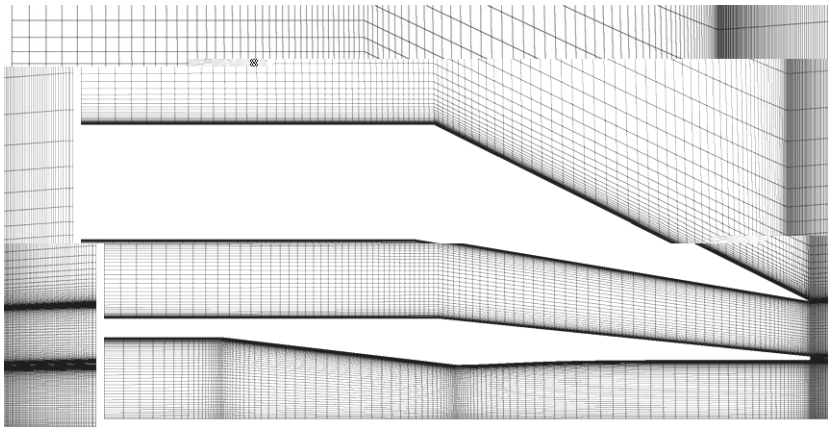

Fig. 17. Computational grid for the C20 coaxial nozzle configuration.

thickness reducing the effective area ratio of the nozzle exit station to the nozzle throat. As a result, a fourth set of calculations was obtained by running the SST model with laminar specification inside the primary and secondary nozzles. Downstream in the jet plume region, the SST model was employed as with the standard case. These calculations obtained with laminar walls resulted in a nearly perfectly expanded nozzle, with the primary nozzle exit Mach number very close to 1.5. As a result of this extra simulation, a total of four turbulence model approaches were employed: (1) SST with turbulent wall boundary layers, (2) SST with laminar wall boundary layers, (3) $k-\varepsilon$ with turbulent wall boundary layers, and (4) EASM with turbulent wall boundary layers. No compressibility corrections were used for these calculations.

Fig. 18 provides a comparison of the centerline velocity decay for the single jet using all of the modeling approaches. It may be observed that all of turbulence models capture the core flow decay reasonably well, although all of the calculations overpredict the jet decay rate. It is interesting to compare these Mach 1.5 single jet solutions to those of the incompressible jets, where the calculated potential core lengths were too long and those of the Mach 2.0 jets, where the calculated potential core lengths were shorter than experimentally measured. The better results obtained here for the Mach 1.5 jets is not due to better representation of the jet fluid dynamics, but rather fortuitous agreement with a jet where moderate compressibility effects offset the deficiencies in the turbulence models with no special compressibility corrections.

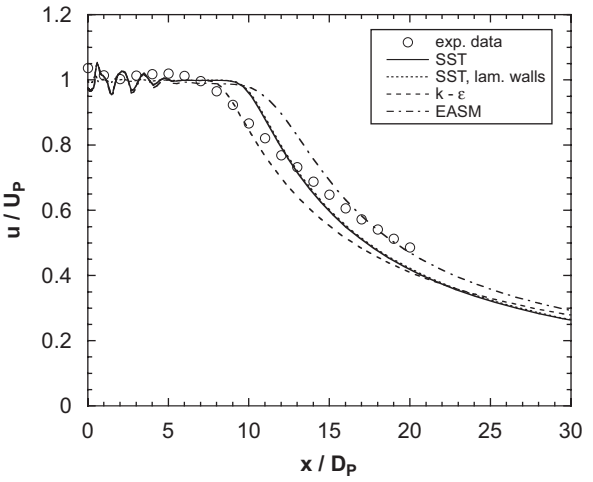

Fig. 18. Centerline velocity decay for Mach 1.5 single jet.

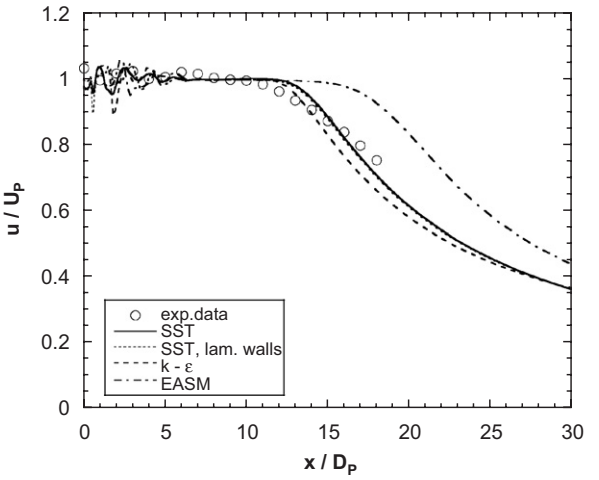

Fig. 19. Centerline velocity decay for the C20M60 coaxial nozzle configuration.

Table 3
Potential core length comparisons

Case	Expt.	SST	SST (lam.)	Chien $k-\varepsilon$	$k-\varepsilon$ EASM
Single	9.2	10.4	10.4	9.0	11.5
C14M37	10.5	10.5	10.5	9.6	12.5
C14M60	11.4	11.4	11.3	10.2	13.4
C14M90	12.5	12.2	12.1	11.1	14.8
C17M37	11.4	11.2	11.1	10.7	13.9
C17M60	13.3	12.9	12.7	11.8	15.7
C17M90	15.1	14.4	14.3	13.3	18.3
C20M37	12.3	11.8	11.7	11.0	14.0
C20M60	13.8	14.2	14.1	13.4	17.9
C20M90	15.5	16.6	16.5	15.5	21.6

The centerline velocities comparisons for one of the coaxial cases, the largest secondary nozzle geometry with Mach 0.60 secondary flow (C20M60), is shown in Fig. 19. Here it may be observed that each of the linear two-equation models predicts the lengths of the primary jet potential core in close agreement to the experimental data, while the EASM solution indicates a significantly longer potential core. It may be noted that for all of the results presented in Figs. 18 and 19, there are no notable differences between the standard SST calculations and the calculations using the modified SST approach with laminar walls, except for differences just downstream of the nozzle exit plane. The qualitative agreement of the

calculations using the four turbulence modeling approaches for the other coaxial configurations and secondary flow Mach numbers is similar to that of the C20M60 results shown in Fig. 19. In the interest of space, all of these results are not presented in this article, but may be found in Ref. [67].

However, a comparison of the primary flow potential core lengths obtained from the experiment and calculations for each of the 10 flow cases is presented in Table 3. In Ref. [8] the velocity potential core length was defined as the distance from the nozzle exit to the location where the velocity is 90% of the primary jet exit velocity:

$$\frac{u(x)}{U_{\mathrm{P}}} = 0.9. \tag{45}$$

The results shown in Table 3 indicate that the three linear two-equation turbulence model approaches indicate reasonably close agreement with the experimental data. The Chien $k-\varepsilon$ results indicate a slightly shorter core than the SST solutions as was the case for the other configurations examined in this article. The potential cores of the SST and SST (with laminar boundary layers) solutions are extremely similar, indicating that the differences in the upstream wall boundary layers and resulting state of the primary jet core flow at the nozzle exit are not as significant as jet mixing effects.

It may be noted that the EASM solutions indicate significantly longer potential cores than those of the other turbulence models and the experimental data. Despite the greater sophistication of the EASM, similar results were obtained for the lobed nozzle calculations. It was concluded that a recalibration of the particular EASM used there (same $k-\varepsilon$ based EASM as used here) for jet mixing problems was required, as is supported by these results. Following such a recalibration, the benefits of the EASM, in particular the capability to model turbulent flow anisotropies, may be realized.

Detailed comparisons of velocity profiles are provided for the single jet in Fig. 20 and the C20 coaxial nozzles in Fig. 21 at 5 axial stations in the jet development region. These comparisons further indicate the overall good agreement between calculations provided by the SST linear two-equation turbulence model and the experimental data.

More extensive comparisons of the computations with experimental data are provided in Ref. [67]. The experiments of Ref. [8] did not make measurements of turbulent statistics, but considering the reasonable agreement between the computations

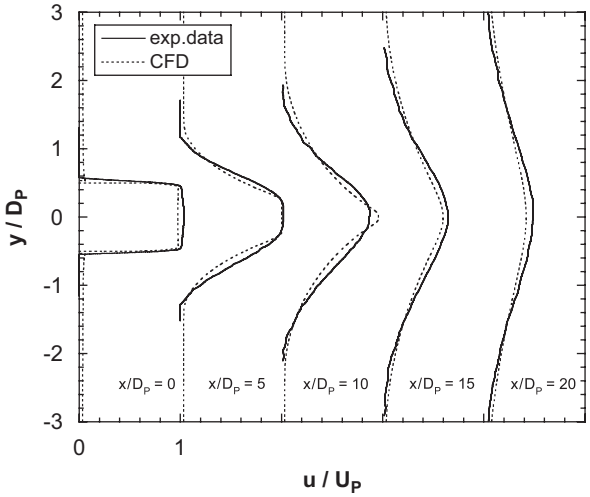

Fig. 20. Velocity profiles for Mach 1.5 single jet.

and experiments for mean velocities as described here, the turbulent fields generated by the computations were used to provide further qualitative comparisons among the nozzle geometric configurations and operating conditions that were varied.

2.5.2. Eccentric-coaxial nozzle comparisons

As mentioned earlier, eccentric nozzles were considered in addition to the coaxial nozzle configurations in the experiments of Ref. [8]. One of the eccentric nozzles was examined in the computations of Ref. [68] having $D_{\mathrm{S}}/D_{\mathrm{P}} = 1.7$. Two secondary Mach numbers were considered, Mach 0.60 and Mach 0.90. As a result, the eccentric nozzle cases discussed here are designated as E17M60 and E17M90 in notation analogous to that described previously for the coaxial configurations.

Fig. 22 shows a view of the grid topology used for the eccentric grid. It may be observed here that the primary nozzle is translated vertically upward to nearly touch the secondary flow nozzle at the nozzle exit plane. For the coaxial and eccentric nozzle cases investigated here, the grids extended 60 D_{P} downstream from the nozzle exit and 24 D_{P} vertically from the primary jet centerline.

To begin examination of the coaxial and eccentric nozzle flowfields, we compare the experimentally measured and computed centerline velocities for the Mach 0.60 and Mach 0.90 secondary flow cases in Fig. 23. The Menter SST model was used for the calculations described here. Although the computations do not match the experimental measurements, the experimentally observed trends of the eccentric

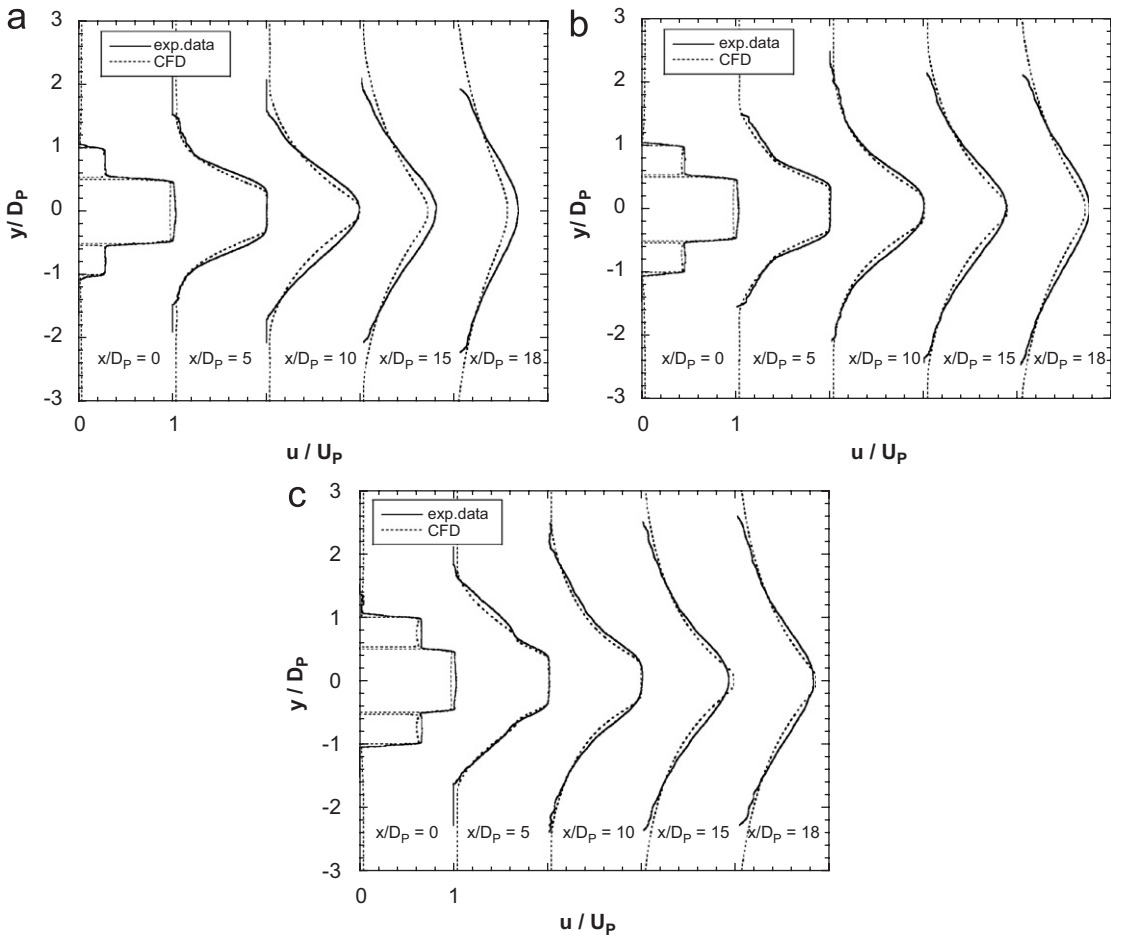

Fig. 21. Velocity profiles for C20 coaxial jets. (a) Mach 0.37 secondary flow. (b) Mach 0.60 secondary flow. (c) Mach 0.90 secondary flow.

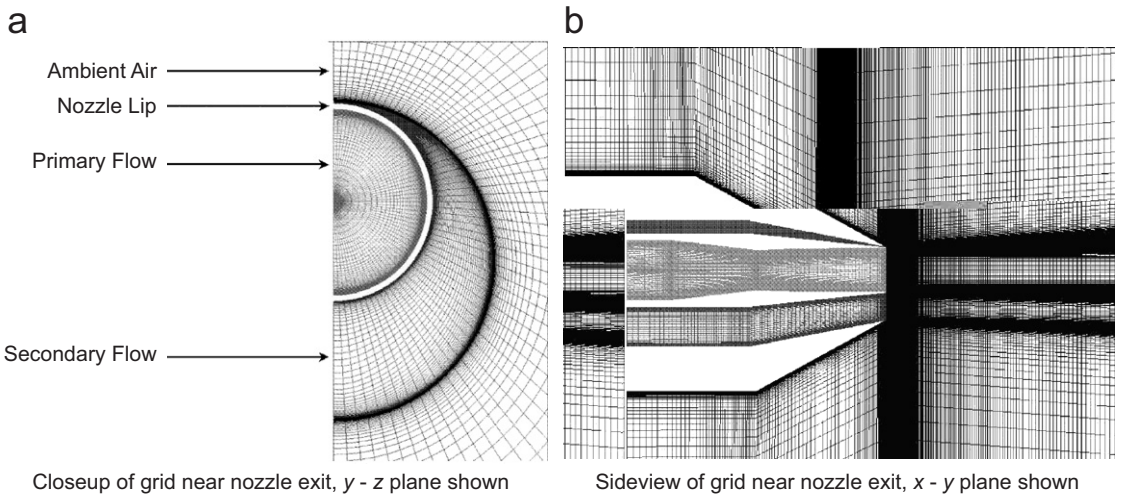

Fig. 22. Computational grid for the eccentric nozzle arrangement. (a) Closeup of grid near nozzle exit, $y-z$ plane shown. (b) Sideview of grid near nozzle exit, $x-y$ plane shown.

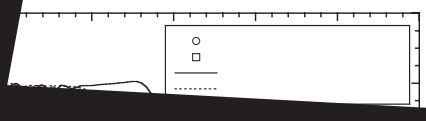

having a faster initial deca
axial jet (for the same sec
ons) is also observed in the co
The computations generally i
mary jet potential core lengths tha
experiment, but Table 4 shows tha
tions do reflect the trends of the exp
comparing the coaxial and eccentric c
It may also be noted that the centerline
the axial velocity with axial position, x/D
jet exit is much higher in the computatio
the experiment. These oscillations are du
imperfectly expanded primary jet underg
series of mild compressions and expansions
jet mixing region develops. It is believed tha
experimental data does not indicate the s
magnitude of the oscillations due to the assumpt
of constant static pressure in the experiment
measurement system. It is also interesting to note
that the coaxial jet with Mach 0.90 secondary
flow experiences the largest oscillations of any case.
This is the result of the supersonic primary jet,

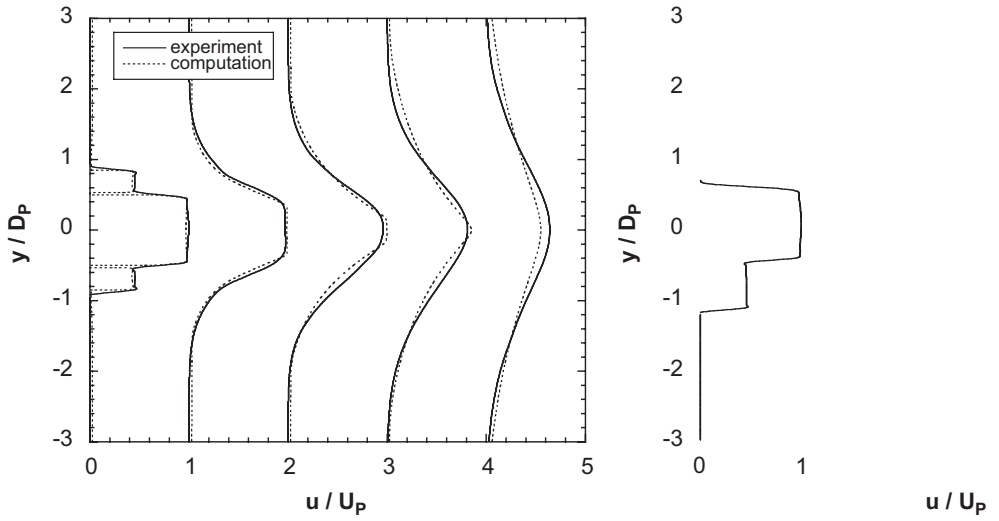

equations in a time accurate manner without approximation. In order to obtain an accurate representation of the turbulence, the turbulent motion down to the Kolmogorov scales must be accurately resolved in both time and space. In other words, the grid spacing must be no larger than the Kolmogorov scale, κ. In order to resolve just one large scale eddy we would need ℓ/κ grid points in each direction, a total of $Re_t^{9/4}$ points. The amount of computer memory available limits the size of the computational grid that can be used and the computer's processing speed gives a practical limit to the number of time steps possible in a simulation. Therefore, based on available computational resources, DNS is limited to very low Reynolds number flows.

Freund [69–71] has computed Mach 0.8, 0.9, and 1.92 jets using a DNS technique. These jets had Reynolds numbers of 800, 3600, and 2000, respectively. This work has produced excellent agreement with experimental data and provided great insight into the flow behavior. But the Reynolds numbers

of the jets are orders of magnitude smaller than any nozzle of practical interest.

The Navier–Stokes equations are presented below. It is these equations that are solved in DNS, without any approximation, such as the Reynolds averaging that produces Eqs. (1)–(3) or filtering (discussed in the next section) that produces the LES equations. They express the conservation of mass, momentum, and energy for an unsteady compressible fluid in tensor form using cartesian coordinates (x_i):

$$\frac{\partial \rho}{\partial t} + \frac{\partial}{\partial x_i}(\rho u_i) = 0, \tag{46}$$

$$\frac{\partial}{\partial t}(\rho u_i) + \frac{\partial}{\partial x_j}(\rho u_i u_j) + \frac{\partial P}{\partial x_i} - \frac{\partial \tau_{ij}}{\partial x_j} = 0, \tag{47}$$

$$\frac{\partial(\rho e_t)}{\partial t} + \frac{\partial}{\partial x_j}(u_j(\rho e_t + P)) - \frac{\partial}{\partial x_j}(u_i \tau_{ij}) + \frac{\partial q_j}{\partial x_j} = 0. \tag{48}$$

3.2. Large-eddy simulation

3.2.1. Filtering process

The basis of LES is the separation of the large and small scale turbulent fluctuations. To separate the large (resolved) and small (unresolved) scales, the equations are filtered. A spatial filter G with a filter width Δ is used:

$$\bar{f} = \int_{-\infty}^{\infty} G(x-\xi) f(\xi)\, \mathrm{d}\xi. \tag{49}$$

The overbar represents the resolved, filtered, or large-scale portion of the function. Commonly used filter functions are a box filter, a Gaussian filter, or a spectral cutoff filter [72]. Typically, it is not necessary to know the exact form of the filter function G, but only that it exists. In practice, the solution is not explicitly filtered. It is assumed that the numerically computed solution is a filtered representation of the exact solution.

Several constraints are imposed on the filter function.

(1) $G(-\xi) = G(\xi)$.
(2) $\int_{-\infty}^{\infty} G(\xi) d\xi = 1$.
(3) $G(\xi) \to 0$ as $|\xi| \to \infty$.
(4) $G(\xi)$ is small outside $(-\Delta/2, \Delta/2)$.

These constraints are necessary to insure that the filter function will commute with the derivative:

$$\frac{\overline{\partial f}}{\partial x} = \frac{\partial \bar{f}}{\partial x}. \tag{50}$$

Favre (density) weighting is frequently used in the filtering process. This allows for convenient recovery of terms corresponding to the unfiltered equations.

$$\tilde{f} = \frac{\overline{\rho f}}{\bar{\rho}}. \tag{51}$$

The filtering process is applied to the continuity, momentum, and energy equations. The resulting equations are composed of resolved and unresolved terms. The resolved terms in the filtered equations directly correspond, in form, to the unfiltered equations.

The resulting LES expressions for conservation of mass, momentum, and energy are

$$\frac{\partial \overline{\rho}}{\partial t} + \frac{\partial}{\partial x_i}(\overline{\rho}\tilde{u}_i) = 0, \tag{52}$$

$$\frac{\partial}{\partial t}(\overline{\rho}\tilde{u}_i) + \frac{\partial}{\partial x_j}\left(\overline{\rho}\tilde{u}_i\tilde{u}_j\right) + \frac{\partial \overline{P}}{\partial x_i} - \frac{\partial \overline{\tau}_{ij}}{\partial x_j} - \frac{\partial \tau_{ij}^{\mathrm{sgs}}}{\partial x_j} = 0, \tag{53}$$

$$\frac{\partial}{\partial t}(\overline{\rho}\tilde{e}_t) + \frac{\partial}{\partial x_j}(\overline{\rho}\tilde{u}_j\tilde{e}_t + \tilde{u}_j\overline{P}) - \frac{\partial}{\partial x_j}(\tilde{u}_i\overline{\tau}_{ij} + \tilde{u}_i\tau_{ij}^{\mathrm{sgs}}) + \frac{\partial}{\partial x_j}(\overline{q}_j + q_j^{\mathrm{sgs}}) = 0. \tag{54}$$

Recalling Eqs. (1)–(3) in the RANS section, the terms denoted with a hat were mass-weighted, time-averaged quantities. All turbulent effects, i.e. the turbulent stress, τ_{ij}^{T}, and the turbulent heat flux, q_j^{T} were replaced with a turbulence model. In Eqs. (52)–(54), the terms denoted with a tilde are mass-weighted, spatially filtered quantities. The sub-grid scale (SGS) stress, τ_{ij}^{sgs}, and the SGS heat flux, q_j^{sgs}, also are replaced with a model. The modeled SGS stresses, however, are only those that are too small to be resolved by the computational scheme and grid.

3.2.2. SGS modeling

The unresolved or SGS contributions must be modeled. To illustrate the sub-grid modeling process, the widely used SGS model of Smagorinsky [73] will be described. Additional terms to account for compressibility were added based on the work of Moin et al. [74]. More complex sub-grid models will be discussed in a later section. The compressible form of the Smagorinsky model, given by Moin

et al., is shown here

$$\tau_{ij}^{\mathrm{sgs}} = -2\overline{\rho}C(\Delta)^2|S|(\tilde{S}_{ij} - \tfrac{1}{3}\tilde{S}_{kk}\delta_{ij}) + \tfrac{2}{3}C_I\Delta^2\overline{\rho}|S|^2\delta_{ij}, \quad (55)$$

where the strain rate, $\tilde{S}_{ij}$ is given by

$$\widetilde{S}_{ij} = \frac{1}{2}\left(\frac{\partial\widetilde{u}_j}{\partial x_i} + \frac{\partial\widetilde{u}_i}{\partial x_j}\right). \quad (56)$$

And further, the magnitude of the strain rate, $|S|$, is obtained from

$$|S| = \sqrt{2\tilde{S}_{ij}\tilde{S}_{ij}}. \quad (57)$$

The parameter Δ is the length scale used in the spatial filtering of the equations and as a result is used as the characteristic length scale of the sub-grid turbulence. Typically, Δ is taken to be the grid spacing. In a three-dimensional computational grid with unequal spacing in each direction, this sub-grid length scale is frequently defined as

$$\Delta = (\Delta x\Delta y\Delta z)^{1/3}. \quad (58)$$

The constants C and C_I have been found to be dependent on the flow under investigation. Rogallo and Moin [75] suggest a range for C in the range $0.01 \leqslant C \leqslant 0.0576$ and for C_I in the range $0.0025 \leqslant C_I \leqslant 0.009$, but several authors, including Moin et al. [74], Ragab [76] and Choi et al. [77] mention that the contribution of the term involving C_I may not be important for flows without significant compressibility and may be neglected.

With this approximation, the SGS stress can be written analogously to the turbulent Reynolds stress of the RANS equations:

$$\tau_{ij}^{\mathrm{sgs}} = -\mu_t(\tilde{2}S_{ij} - \tfrac{2}{3}\tilde{S}_{kk}\delta_{ij}), \quad (59)$$

where the SGS eddy viscosity is given by

$$\mu_t = \overline{\rho}C(\Delta)^2|S|. \quad (60)$$

Finally, the SGS heat flux is modeled analogously to that done for the turbulent heat flux of the RANS equations:

$$q_j^{\mathrm{sgs}} = -k_t\frac{\partial\tilde{T}}{\partial x_j}, \quad (61)$$

where k_t is related to μ_t through the turbulent Prandtl number.

While the LES equations are analogous in form to their RANS counterparts, they are very different in application. The LES equations are solved in a time accurate manner and significant unsteady motion should be present. In RANS, the effect of the eddy viscosity dominates the flowfield while in LES, the eddy viscosity has a much smaller effect.

4. Examples of LES of jet flows

Jet flows have been a popular application of LES. This section summarizes a representative sample of the work to date. Much of the work has focused on unheated round jets, the exceptions to this are noted.

Lele and coworkers performed several simulations of hot and cold Mach 0.9 jets at low to moderate Reynolds number using a consistent approach [78–80]. They employ a sixth-order compact differencing in space [81] and an explicit low-dispersion Runge–Kutta (LDRK) differencing in time. They use a dynamic sub-grid model and the solution is explicitly filtered. The inflow boundary condition consists of a velocity profile with sinusoidal forcing of the axial velocity component and random forcing of the azimuthal velocity component.

Bogey and Bailly have simulated several subsonic jets [82–84]. Their method uses 13 point finite-differencing in space. The finite difference stencil is optimized to minimize the dispersion error and is based on Tam and Webb's dispersion relation preserving (DRP) scheme [85]. They also use a LDRK scheme for time advancement. Their earlier work employed explicit modeling of the SGSs. However, recent work has relied on filtering without sub-grid models. They have also examined the influence of eddy viscosity on the effective Reynolds number of the flow.

Shur, Spalart and Strelets have taken a different approach [86,87]. They have adapted a RANS code which uses a finite volume approach employing the Roe scheme. The fluxes are computed with hybrid fifth-order upwind/fourth-order central differences. Limiters are used in the presence of shocks. Time advancement is done using an implicit second-order scheme. This simulation does not use a SGS model. They rely on the numerical dissipation of the scheme to remove energy that would be dissipated by the small scales. The authors have simulated a chevron nozzle by modifying the inflow boundary condition and altering the grid at the inflow plane.

These simulations all utilized an inflow boundary condition that specifies the jet velocity profile. The velocity profiles are typically represented using a hyperbolic tangent function. With the exception of Shur, Spalart and Strelets, some type of unsteady

perturbation is typically imposed. The development of the shear layer is dependent on the initial shear layer thickness as well as the type, frequency and magnitude of the imposed velocity perturbations. Because turbulence data near the nozzle exit is difficult to obtain, the inflow boundary is usually assumed to be at an unspecified location downstream of the nozzle exit. To compare with experimental data the results of the analysis are usually shifted along the jet axis so that the end of the potential core in the experiment and LES match.

In their review paper, Bodony and Lele [88] presented a comparison of several predictions of axial velocity and axial velocity root-mean-square on the jet centerline for several different speed jets. A representative sample at Mach 0.9 for both cold and hot jets are shown in Figs. 26 and 27. The predictions were supplied by several leading researchers in jet LES and the details of their methods varied greatly. The

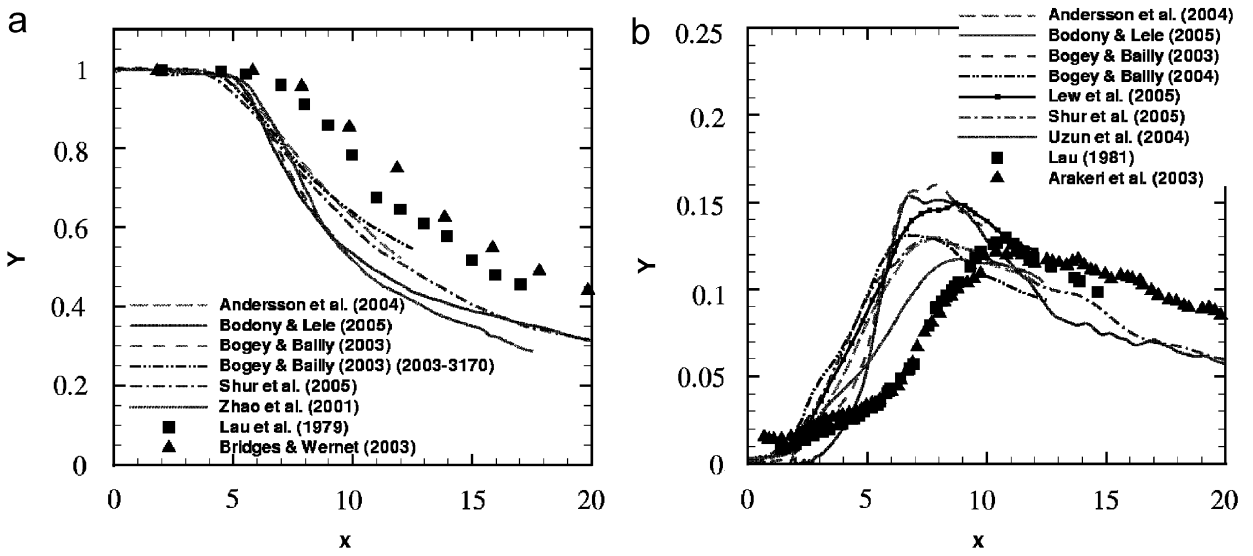

Fig. 26. Comparison of predictions of centerline axial velocity for a cold Mach 0.9 jet (from [88]). (a) Mean velocity. (b) Root-mean-square velocity.

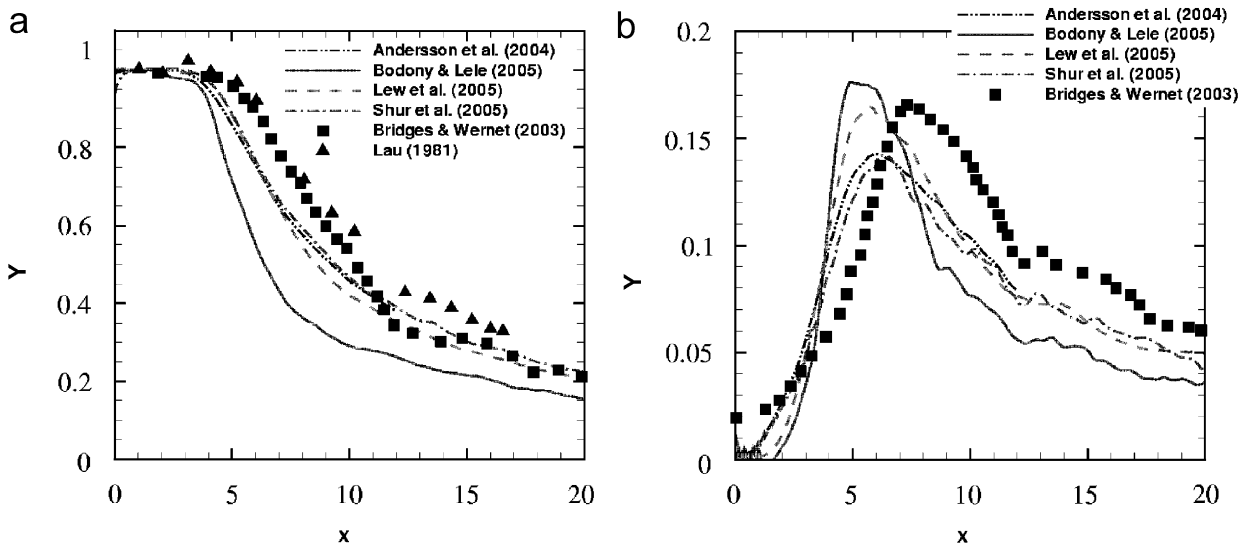

Fig. 27. Comparison of predictions of centerline axial velocity for a hot Mach 0.9 jet (from [88]). (a) Mean velocity. (b) Root-mean-square velocity.

Fig. 28. Pre

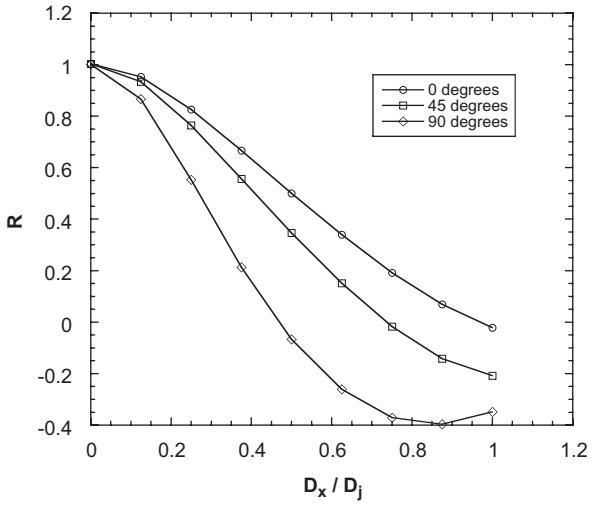

Fig. 30. Two point space correlation coefficient from a Mach 1.4 jet.

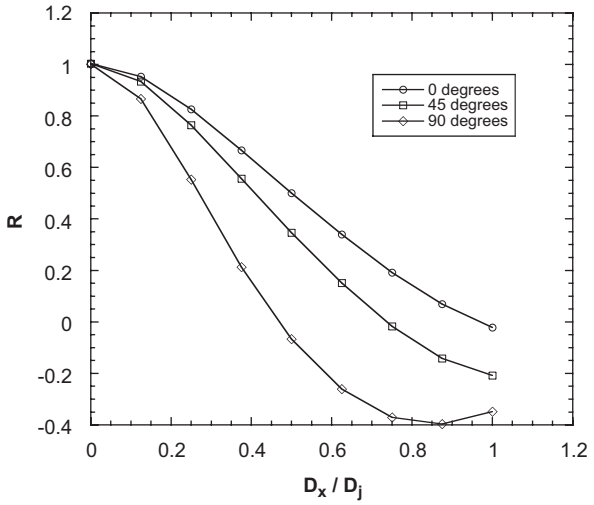

Fig. 31. Convection velocity from a Mach 1.4 jet.

downstream development of the jet, and that it is most important to correctly model the bulk properties of the initial shear layer. This approach eliminates the uncertainty in the origin of the jet exit. Centerline velocity profiles for the supersonic and subsonic jets are shown in Fig. 28. For the supersonic case a comparison is made of two solutions in which the number of azimuthal grid planes was varied. For the subsonic case the effect of the coefficient in the Smagorinsky sub-grid model was studied.

Paliath and Morris [94] performed a simulation which combined both approaches. The nozzle was included in the simulation to obtain the correct bulk properties of the boundary layer/initial shear layer. They also imposed small perturbations in the shear layer to simulate the small-scale turbulence that could not be modeled. Their analyses included both round and rectangular nozzle geometries.

DeBonis's results also demonstrated the ability of LES to produce more detailed turbulent information. In this case, two-point space and space-time correlations were obtained for both the supersonic and subsonic jets as shown in Fig. 29. These statistics are important for the construction of acoustic source models for jet aeroacoustic analysis. The correlations of u' and u'^2 are used to compute the shear and self-noise components, respectively. The figures show the correlation of u' in the jet mixing layer near the end of the potential core for several separation distances. For the supersonic case, two-point space correlations were used to estimate a turbulent length scale (Fig. 30) and the space–time correlations were used to estimate a convection velocity (Fig. 31).

4.1. Approaches to LES of jet flows

There appears to be two general philosophical approaches to the application of LES to jet flows, the rigorous and the practical. Both approaches have yielded reasonable results in their targeted application.

4.1.1. Rigorous LES

The approach which will be called rigorous LES, involves careful attention to all aspects of the LES procedure. Each part of the LES solution is explicitly addressed: numerical error, filtering and sub-grid modeling. Careful attention is paid to minimizing numerical error. High-order schemes which minimize dispersion and dissipation errors are used. Explicit filtering of the solution is typically performed. The filtering process removes the small unresolved scales from the solution in a mathematically consistent manner and has the added benefit of enhancing numerical stability. The subgrid scale stresses are modeled using any one of a number of sub-grid models. These calculations are typically performed for very low Reynolds number round jets. In addition these approaches have traditionally been used for simple geometries. A low Reynolds number flow has a narrower range of turbulent scales and enables better resolution, decreasing the importance of the sub-grid model. The benefit of this approach is the ability to evaluate and control

the contributions of each solution component. The drawback is the cost and complexity of the system.

4.1.2. Practical LES

Practical LES takes a more pragmatic approach, attempting to get a reasonable answer with less regard to every detail of the analysis (this is not a statement on the quality of the work). Instead of separate components for filtering and sub-grid modeling, one or both of these are usually combined with the numerical scheme. More dissipative schemes such as those found in most RANS codes are used. These analyses are usually performed for complex geometries and at high Reynolds number. More empiricism may be needed to achieve a good solution. Many simulations which fall into this category use codes that have been adopted from RANS. In these cases, the codes have more flexible grid requirements and complex geometries are easier to model.

5. Key issues in LES simulations

5.1. Numerical scheme

The numerical scheme plays a major role in the simulation's accuracy and can have a significant effect on how the other components of the simulation work. A wide variety of numerical schemes have been employed for LES of jet flows. A large majority of LES has been performed using schemes that have a high-order of accuracy.

5.1.1. Explicit finite difference schemes

Explicit finite difference methods include both the traditional finite difference stencils and the optimized DRP type schemes. For a traditional finite difference stencil the coefficients are chosen to maximize the order of accuracy of the scheme. Newer optimized stencils are based on Tam and Webb's DRP scheme [85]. In this method, the order of accuracy does not determine the stencil coefficients. Instead, the coefficients are chosen to minimize the error of the scheme over a limited range of wave numbers. Optimized schemes are a good choice for LES. Since the range of scales that must be resolved is finite, it makes sense to minimize the error over this range. Furthermore it must be pointed out that a numerical scheme's order of accuracy only indicates how the error will be reduced with grid refinement and does not indicate the magnitude of the error for a given grid size. Tam and Webb's original DRP scheme uses a seven point stencil. Bogey and Bailly's scheme uses a 13 point stencil [95]. Such a wide stencil makes implementation of the scheme difficult near boundaries and block interfaces.

5.1.2. Compact schemes

Compact schemes implicitly compute the derivative [81,96,97]. An example of a sixth-order compact scheme which results in a tridiagonal system is shown [98].

$$\frac{1}{15}(14\delta_{2x}f_j + \delta_{4x}f_j) = \frac{1}{5}\left[\left(\frac{\mathrm{d}f}{\mathrm{d}x}\right)_{j+1} + 3\left(\frac{\mathrm{d}f}{\mathrm{d}x}\right)_j + \left(\frac{\mathrm{d}f}{\mathrm{d}x}\right)_{j-1}\right]. \quad (62)$$

This enables more accurate schemes for a given size stencil. In addition, these schemes have excellent resolution in wave number space. Their implicit nature increases the complexity and computational cost of the scheme. But, the narrow stencil aids in implementation near boundaries and block interfaces. Some codes utilizing compact schemes for jet analyses have been developed by Lele [81], Gaitonde and Visbal [99], and Hixon [96].

5.1.3. Artificial dissipation/filtering

The schemes discussed so far are central difference formulations. This is done to eliminate the dissipative error terms and preserve the turbulent structures. The lack of inherent dissipation in the scheme means that the solution will be unstable. Artificial dissipation, frequently in the form of a filter, is added to maintain stability. Compact filters have been developed by Lele [81], Gaitonde and Visbal [97] and Hixon [100]. Other filters have been developed by Kennedy and Carpenter [101], Vasilyev [102] and Bogey and Bailly [95]. These schemes do not capture shocks well and they have been applied primarily to subsonic jets. Some work has been done to improve shock capturing by combining filters; a switch, typically based pressure gradient, is used to apply the more dissipative shock capturing filter near the shock and apply the less dissipative filter elsewhere [103,104].

5.1.4. Upwinded schemes

The vast majority of modern CFD codes are finite volume RANS solvers utilizing upwinded schemes such as the popular Roe scheme [105]. Upwinded schemes are dissipative and tend to damp turbulent

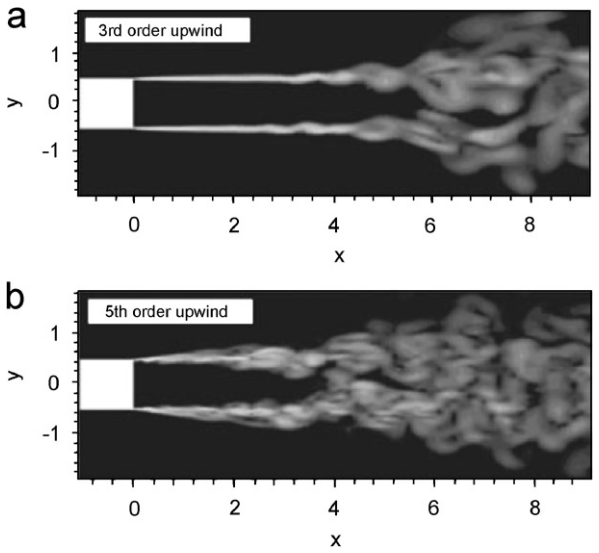

Fig. 32. Effect of numerical dissipation on resolution of turbulent scales (from [86]). (a) Third-order upwind. (b) Fifth-order upwind.

structures that LES hopes to capture. Such general purpose solvers may not be immediately appropriate for high quality LES run in the same manner as RANS. However, by increasing the order of the schemes, and subsequently reducing the amount of dissipation, they have proven successful in some implementations [86,87]. They are particularly suited for the monotonically integrated large-eddy simulation (MILES) approach [106,107].

The importance of the spatial discretization scheme in LES cannot be overstated. As illustration, Fig. 32 shows the difference between two numerical schemes with differing amounts of dissipation. The simulation approaches, from Shur, Spalart and Strelets [86], are identical except for the fact that the first uses a third-order upwinded scheme and the second uses a fifth-order upwinded scheme. The latter scheme has significantly less dissipation and therefore has better resolution of the turbulent structures.

5.1.5. Temporal discretization

A lot of attention has been focused on the proper spatial discretization for LES. In contrast, relatively little effort has been given to the temporal scheme. Some work has been done examining the error due to the temporal discretization on numerical solutions in one-dimension [108] where it was shown that the order of the numerical scheme was determined by the lower-order discretization (temporal or spatial). A high-order spatial discretization can be comprised by the error of a lower-order temporal scheme. This has not been extended to multiple dimensions where additional errors in the spatial discretization complicate matters. Explicit Runge–Kutta schemes are used for most analyses; typically combined with compact or explicit finite difference schemes. Both the standard four-stage fourth-order scheme [109] and optimized low-dissipation and low-dispersion schemes are used [110–112]. The optimized schemes add additional stages to reduce error. Regardless of the scheme it is prudent to perform a simple check of the effect of the temporal discretization error by repeating a portion of the calculation using a smaller time step.

5.2. Grid

Grid requirements will obviously vary based on the numerical scheme used. Issues such as the number of grid points required, grid skewness, and the allowable rate of grid stretching are highly dependent on the individual numerical method. Some but not all researchers have attempted to quantify these requirements for their particular schemes. Ideally isotropic grids would be used for these calculations. But, computing limitations force the implementation of grid stretching to cluster points in the regions of interest.

Many analysis codes used for jet LES have limited geometric flexibility. Most written for jet analyses have used a cylindrical coordinate system, a natural choice for a round jet. Others have used a cartesian system for simplicity in the numerical implementation [113,114]. As the technology begins to move beyond studies of simple round jets it will be necessary to add geometric flexibility by adopting generalized curvilinear coordinates. This will enable a transition to studies of more realistic nozzle systems with complex geometries.

Generalized curvilinear coordinates may not be enough to tackle the most difficult nozzle systems. RANS analyses of complex nozzle systems use flexible multi-block grids with varying topologies [31,40,115,116]. LES simulations can utilize multiple grid blocks to enable parallel computation. But the grid blocks are subdivided from a single grid, which enables simple point matched interfaces through overlapping or ghost cells. Block interfaces that maintain high-order of accuracy must be developed.

Non-point matched interfaces will be very useful for geometry modeling and to coarsen the grid away from regions of interest.

Unstructured grids offer a solution to the difficulties faced in multiblock structured grids. However, developing high-order schemes for unstructured grids is a difficult task. Some work has begun in this area [117–119]. There is a lot of work to be done before this technology can be utilized for jet flow analyses.

Pope advocates the use of solution adaptive gridding to eliminate the subjective specification of the resolved turbulent length scale [120]. This idea is an excellent way to insure proper resolution, but it will place a great dependence on increased grid flexibility in LES codes.

5.3. Boundary conditions

5.3.1. Outflow boundary

There have been two on-going issues regarding boundary conditions for jet LES. The first is a non-reflecting outflow boundary condition. Waves that reflect from the outflow back into the computational domain can contaminate the solution. There are many self-contained boundary conditions written to eliminate these reflections using characteristic wave relations [121–124]. These methods have had moderate success but can be difficult to implement in a general way. Many researchers have had success with the more ad hoc approach of creating what is referred to as absorbing layers/sponge regions/exit zones near the boundary [125]. These are areas of gradually increasing grid spacing. The increased grid spacing combined with dissipation of the numerical scheme serves to damp waves as they near the boundary. Additional dissipation or source terms in the governing equations are sometimes added to increase the damping.

5.3.2. Specification of the jet

The second boundary condition issue, the inflow boundary, is one of the most important needs for LES of complex nozzle systems. The method used to specify the jet is critical to the downstream development of flow structures. A common approach to specifying the inflow is through a velocity profile. The profile is frequently based on a hyperbolic tangent function and the initial mixing layer thickness is specified. An unsteady component can be added to simulate the initial turbulence levels. This artificial "forcing" of the shear flow can greatly influence the mixing of the jet. Great care must be taken to avoid biasing the solution and adversely affecting the acoustic farfield. Glaze and Frankel found that random fluctuations based on a Gaussian distribution dissipated quickly downstream [114]. Bogey and Bailly studied both the effects of forcing different modes and the effect of shear layer thickness, with significant differences in results [113].

The initial mixing layer thickness affects the stability of the flow and also has a great effect on the jet development. Shur, Spalart and Strelets [86] argue that this is the primary mechanism in the transition from small-scale to large-scale turbulence in the jet and that the small-scale turbulence from the nozzle boundary layer has only a weak effect. They do not use forcing and have had good success. DeBonis [92,93] included the nozzle geometry in the grid. These simulations resulted in realistic boundary-layer thicknesses at the nozzle exit, but the grid spacing was not sufficient to capture the small-scale turbulence. These simulations also showed reasonable success without forcing.

To accomplish the goal of producing predictions of nozzle systems with acoustic suppression devices, a hybrid RANS/LES approach is a promising option. In this approach the nozzle geometry is included in the simulation and the flow exiting the nozzle is directly computed, removing the assumptions involved in specifying a velocity profile. Correct modeling of the boundary layer on the internal nozzle surface is critical. LES of the small turbulent structures in the boundary layer is prohibitive due to the very fine grid necessary. A hybrid RANS/LES approach can accurately capture the bulk properties of the boundary layer. However, unsteady information for the LES of the jet cannot be provided directly from the RANS simulation of the boundary layer. There are several approaches to interface the RANS to LES regions. As with an inflow boundary condition, randomly generated turbulence which is scaled to match the RANS turbulent kinetic energy is quickly dissipated. Batten et al. [126] have developed a method which generates velocity fluctuations at the interface that satisfy a target set of time and length scales from the given RANS statistics. Others have used the concept of recycling, scaling the results of a previously run LES simulation of a boundary layer to match the RANS simulation and imposing them on the interface [127,128].

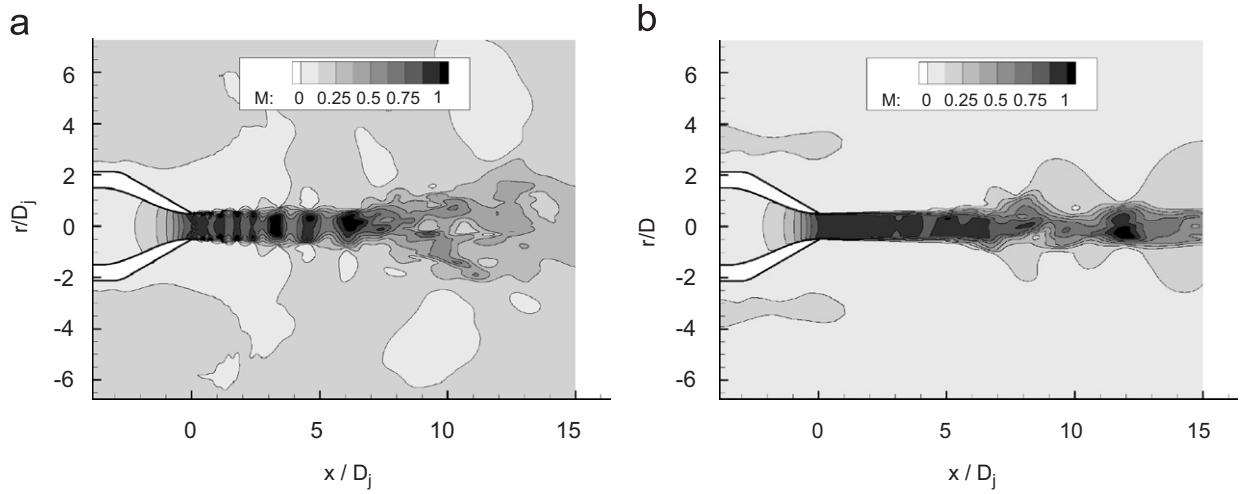

Fig. 33. Effect of sub-grid model on resolution of turbulent scales. (a) Mach contours using Smagorinsky coefficient $C = 0.012$. (b) Mach contours using Smagorinsky coefficient $C = 0.10$.

5.4. Sub-grid modeling

There are numerous approaches to sub-grid modeling, many of which have been applied to jet flows with success. Piomelli has an excellent discussion of the types of SGS models in his review paper [129]. This explicit modeling of the SGSs has been the traditional approach. Recently, there have been several works where the sub-grid stresses have been represented implicitly by dissipation inherent in the filter or numerical scheme. Bogey and Bailly forego sub-grid modeling and rely on the dissipative effect of an explicit filter to remove energy from the large scales [113]. Shur, Spalart and Strelets also use no sub-grid modeling, relying on the dissipation present in their hybrid upwinded scheme [86,87]. The success of the MILES approach also indicates that the details of the sub-grid model are unimportant. In some circumstances sub-grid modeling may be detrimental. Bogey and Bailly have found that the added viscosity from a sub-grid model effectively decreases the Reynolds number of the flow; altering the mean axial velocity, turbulence intensity and sound spectrum [130].

Explicit sub-grid models are formulated with a physics based approach. The dissipation they produce is based on the resolved motion in the simulation and the filter width (typically the grid size). Implicit sub-grid modeling relies on the dissipation from the numerical scheme and is not related to the resolved motion in any physical way. Explicit models should provide the proper amount of dissipation within a range of grid resolution where the flow is properly resolved. There is no basis to assume an implicit sub-grid modeling approach will provide the proper dissipation at different levels of resolution. In other words, the results from a simulation using explicit sub-grid modeling should be expected to improve with grid resolution. The results from a solution using an implicit approach should not have the same expectation.

The effect of the sub-grid model can be seen in the solution of a high Reynolds number Mach 0.9 jet (Figs. 28 and 33) [93]. The method for both solutions was identical save for the coefficient in the Smagorinsky sub-grid model [73]. The first solution uses the generally accepted "standard" value of 0.012 (Fig. 33(a)). This solution shows a very energetic flowfield with numerous small-scale eddies. The mean centerline velocity profile for this solution showed too much mixing, indicating that not enough energy was being dissipated from the large scales. The second solution uses an increased Smagorinsky coefficient of 0.10 (Fig. 33(b)). This solution shows only a few large-scale structures, the Reynolds number effect quantified by Bogey and Bailly. But, the centerline velocity profile is a close match with the experiment (Fig. 28(b)). It is critical that the correct amount of energy is dissipated from the large scales.

5.5. Filtering

The process of filtering the Navier–Stokes equations is fundamental to the development of LES.

The practical need for and implementation of explicit filtering in LES is not clear. Many researchers use the implicit filtering approach. One can argue that the discretization process acts as a filter and no further filtering is necessary [17]. Others explicitly apply a filter to the solution at each time step. Explicitly filtering the solution is the more rigorous approach. But in practical terms, the real benefit of filtering is to provide artificial dissipation for stability, since it removes the small unresolved waves. Successful simulations have been performed with both approaches.

Filtering is a conceptually straightforward process. However, the process becomes more difficult for non-uniform stretched grids. A key to the development of the LES equations is the fact that the filter commutes with the derivative. This is true for uniform grids. Ghosal and Moin defined a new filtering operation which is second-order accurate on non-uniform grids [131]. This error is relatively large compared to the error of high-order schemes. Vasilyev, Lund and Moin developed a class of filters with arbitrary accuracy to enable higher-order solutions [102]. It should be pointed out that these same filters were previously derived by Kennedy and Carpenter without the issue of commutation error in mind [101].

5.6. Matching solution components

A LES code is a combination of many components; numerical scheme, boundary conditions, sub-grid model, filters, etc. An accurate solution can only be had if there is a proper balance among these components. It is not possible to simply hand pick the best components from several different works and expect them to work well together. A good understanding of all the underlying issues is key. In order to strike this delicate balance, a fair amount of empiricism is usually involved. Examples of this include: adjusting the coefficient of the sub-grid model, changing the order of accuracy of the numerical scheme, adjusting the order or coefficient of the filter, selecting the proper grid resolution, and adjusting the incoming jet profile. This is not a criticism of these actions but merely an illustration of the current situation. LES cannot become a predictive tool until this empiricism is removed.

5.7. Reynolds number

The majority of jet LES has been done at low Reynolds number. This significantly reduces the range of turbulent scales and allows for more complete resolution in the analysis. For a given grid size, a low Reynolds number jet will have a greater majority of the turbulent energy directly computed. This means that for a high Reynolds number jet, the contribution of the sub-grid model becomes more important, exacerbating any modeling errors. In some cases, at very high Reynolds number, it is not practical to resolve down to the inertial sub-range region. In these cases, the assumptions upon which most sub-grid models are developed may not apply and the errors in the sub-grid model are increased. While most flows of interest are at high Reynolds number, exploring low Reynolds number jets aids in developing the numerical scheme by providing a resolvable flow-field.

5.8. Evaluation of solutions

LES generates large amounts of information that can be evaluated; not only to gain information on the flow, but also to evaluate the accuracy of the solution. By their nature, the solutions provide high spatial resolution. However, due to the large computational costs involved, the temporal evolution of the flow is usually limited. The small time steps limit the total simulation time to fractions of a second. As computing power is increased, the natural inclination is to increase spatial resolution or increase the complexity of the simulation. It is very important that the simulation has been run "long enough." For all simulations there is a transient period at start-up where the turbulence is developing. During this period, especially near the end of this period, the solution may look realistic. However, the statistics obtained will vary in time. It is important to make sure that the statistics are invariant with time. Rules of thumb such as 2 or 3 "flow-through" times have been cited. But these are ad hoc recommendations and are not a substitute for analysis to insure accurate statistics.

As previously mentioned, analysis of the temporal error should be carried out by repeating a portion of the calculation at a reduced time step.

For a RANS analysis, it is common practice to perform a grid resolution study to demonstrate the solution's grid independence. It is not clear that this is practical or even possible with LES. At the current time, most LES calculations push the limits of the available computing power. Grid refinement is not an option in these cases. Grid coarsening is

possible but the results would most likely be unsatisfactory. When grid refinement is possible, it is unclear what will result. As the resolution increases in an LES solution, more and more turbulent structures will be revealed until the Kolmogorov scales are reached and the solution reaches the DNS limit. When the grid is refined, the turbulent structures within the flow will change and the solution will look "different". A time history of velocity at a point should show additional unsteady motion. This small-scale motion serves to dissipate the larger scales and was previously represented by eddy viscosity or numerical dissipation. But, this motion will now directly contribute to the turbulence statistics of the flow. Further refinement will add additional small-scale motion. Its influence on the statistics and large-scale structures will decrease as the energy of these structures is small compared to the large-scales. The limit where this influence becomes negligible is the ideal level of grid resolution. The question remains whether or not this level of resolution is practical for high Reynolds number jets and complex geometries. Also, are solutions at a lower resolution valid if they have an accurate mean flow but have compromised turbulent statistics, due to the effect of sub-grid dissipation?

The high spatial resolution and short temporal resolution is typically opposite of experimental data sets. The limited time history can make it difficult to obtain accurate spectra. It is impractical to replicate the amount of data obtained in experiment; typically thousands of bins of 256 data points. Great care must be taken when comparing statistics between CFD and experiment.

5.9. Experimental data

As mentioned previously, experiment data typically has limited spatial resolution. Many frequently used data sets have only centerline and select radial profiles. Some new experimental techniques have improved greatly on this. PIV [52] and planar doppler velocimetry (PDV) [132] are two examples of new techniques with great spatial resolution. Rayleigh scattering, a density-based point-wise technique, is completely non-intrusive (no probes or particle seeding). This method was used by Panda to experimentally evaluate the implications of Favre averaging [133] and to characterize the initial mixing layer of the jet [134].

In order to improve LES of complex nozzle systems additional information is needed from experiments. Experimental studies typically do not report the nozzle geometry or characterize the flowfield right at the nozzle exit. Nozzle geometry, internal nozzle boundary layer data and turbulence data in the shear layer right at the nozzle exit are important for developing accurate hybrid RANS/LES interfaces.

6. Summary and conclusions

There is a need in the aerospace community for accurate aerodynamic and aeroacoustic prediction tools for exhaust nozzle systems and the turbulent jet flowfields that they produce. Currently Reynolds averaged Navier–Stokes (RANS) methods are used for the vast majority of calculations. Two-equation models, such as k–ε, k–ω, and Menter's SST formulations that all solve for the turbulent kinetic energy, are the most widely used models for nozzle and jet flows. Solutions from these approaches are often used for jet noise predictions utilizing an acoustic analogy approach. It is clear that important details of the jet flow features such as potential core length, jet spreading rate, and turbulent characteristics are not predicted accurately. Further, RANS methods can only provide time-averaged turbulent information. While considering these limitations, RANS methods can frequently capture the trends exhibited by experiments when altering the geometry or flow conditions of the analysis subject. This fact coupled with the fact that RANS solutions are relatively computationally inexpensive means that RANS methods still have a place for designing nozzle systems.

Several modified linear two-equation turbulence models, developed specifically to improve jet flow predictions, were compared to standard RANS turbulence models. These corrections were calibrated specifically for round jets and in general improve the accuracy of the mean velocity field and quantities such as potential core length, but struggle at improving predictions of the turbulent kinetic energy fields. Further, these corrections cannot be applied universally to all flows and great care must be taken when using these corrected models only where they are applicable. Explicit algebraic stress models (EASM) have also been examined for application to jet flows and while these models include additional flow physics such as turbulent anisotropy effects, the results to date have not yielded improved accuracy over linear two-equation models.

RANS methods are a mature technology and further improvements for the prediction of jet flows will be incremental at best. Therefore, we must look to unsteady methods, direct numerical simulation (DNS) and large-eddy simulation (LES), for large advances in accuracy and fidelity. Even with the impressive advances in computer technology, DNS with extreme requirements on grid resolution and resulting computational expense is not viable for realistic geometries and flow conditions for the foreseeable future. LES is the next logical step. There has been a lot of recent work in development and assessment of LES methods for jet flows. To this point the agreement of LES methods with experimental data does not approach the accuracy of RANS for mean flow quantities. In addition the computational cost of LES is much higher than RANS.

As a result, there is still a great deal of work left to be done before LES surpasses RANS as the method of choice for exhaust nozzle and jet flowfield analyses. However, LES does offer the potential for much greater accuracy. In addition, LES can provide a large amount of unsteady turbulent information, which RANS cannot provide. In this article, a survey of LES research as applied to turbulent jet flows was presented. In addition, areas of research that are most critical to the progression of LES towards a useful jet prediction tool were discussed.

Most LES simulations of jets have focused mainly on benchmark experiments of round nozzles for purposes of method and code development and to gain physical insight. Noise suppressing nozzle systems contain complex geometries to modify the jet turbulent structures. Therefore the nozzle geometry itself must be included in the calculation. Additional effort is required to adapt current LES methods to handle such complex geometries. A promising approach is a hybrid RANS/LES simulation where the upstream nozzle wall boundary layers are calculated using RANS and the jet regions employ LES. But, further work must be done to develop the proper interfaces between the RANS and LES regions. LES methods require high-order numerical schemes which do not lend themselves well to complicated grid topologies. As a result, most LES has focused on simple configurations, such as round jets. These methods must be extended to handle complicated grid schemes in order to make LES viable for future work.

Another very important issue in current jet LES is the specification of the jet inflow. Many researchers use a prescribed velocity profile with imposed unsteady forcing. Others have specified the profile without forcing or modeling the nozzle geometry. Correctly specifying the initial shear layer and understanding its effect on the calculation is key to a successful solution.

Finally, in order to create a true predictive capability, the amount of empiricism currently used in LES must be significantly reduced. There are many aspects of the simulation that are currently tailored by the researcher to improve the prediction; grid resolution, inflow boundary profile and forcing, sub-grid model coefficient, filter order and coefficient, numerical scheme, etc. As we gain a better understanding of the various components that make up a LES simulation and as computing power increases to accommodate higher resolution, LES will become a predictive tool for jet flow simulations.

Acknowledgments

The authors would like to thank Dr. Daniel Bodony, Dr. Dimitri Papamoschou, and Dr. Michael Shur for their kind permission to use figures from their work.

References

[1] Janardan BA, Hoff GE, Barter JW, Martens S, Gliebe PR, Mengle V, et al. AST critical propulsion and noise reduction technologies for future commercial subsonic engines separate-flow exhaust system noise reduction concept evaluation. NASA CR 2000-210039; 2000.

[2] Samimy M, Adamovich I, Webb B, Kastner J, Hileman J, Keshav S, et al. Development and characterization of plasma actuators for high speed and Reynolds number jet control. Exp Fluids 2004;37(4):577–88.

[3] Behrouzi P, McGuirk JJ. Jet mixing enhancement using fluid tabs. AIAA Paper 2004-2401; 2004.

[4] Tam CKW, Zaman KBMQ. Subsonic jet noise from nonaxisymmetric and tabbed nozzles. AIAA J 2000;38(4):592–9.

[5] Hileman J, Samimy M. Effects of vortex generating tabs on noise sources in an ideally expanded Mach 1.3 jet. Int J Aeroacoust 2003;2(1):35–63.

[6] Waitz IA, Qiu YJ, Manning TA, Fung AKS, Elliot JK, Kerwin JM, et al. Enhanced mixing with streamwise vorticity. Prog Aerosp Sci 1997;33:323–51.

[7] Papamoschou D, Debiasi M. Mach wave elimination applied to turbofan engines. AIAA Paper 2002-0368; 2002.

[8] Murakami E, Papamoschou D. Mean flow development in dual-stream compressible jets. AIAA J 2002;40(6):1131–8.

[9] Papamoschou D. Noise suppression in moderate-speed multistream jets. AIAA Paper 2002-2557; 2002.
[10] Papamoschou D. A new method for jet noise reduction in turbofan engines. AIAA Paper 2003-1059; 2003.
[11] Papamoschou D, Nishi K. Jet noise suppression with fan flow deflectors in realistic-shaped nozzle. AIAA Paper 2005-993; 2005.
[12] Papamoschou D. Parametric study of fan flow deflectors for jet noise suppression. AIAA Paper 2005-2890; 2005.
[13] Georgiadis NJ, Yoder DA, Engblom WA. Evaluation of modified two-equation turbulence models for jet flow prediction. AIAA J 2006;44(12):3107–14.
[14] Yoder DA. Algebraic reynolds stress modeling of planar mixing layer flows. PhD thesis, University of Cincinnati; 2005.
[15] Kenzakowski DC, Papp JL, Dash SM. Modeling turbulence anisotropy for jet noise prediction. AIAA Paper 2002-0076; 2002.
[16] Kenzakowski, D.C., Shipman, J., Dash, S.M. Turbulence model study of laboratory jets with mixing enhancements for noise reduction. AIAA Paper 2000-0219; 2000.
[17] Wilcox DC. Turbulence modeling for CFD, 2nd ed. DCW Industries; 1998.
[18] Kenzakowski DC, Papp JL. EASM/J extensions and evaluation for jet noise prediction. AIAA Paper 2005-0419; 2005.
[19] Kenzakowski DC. Turbulence model improvements for jet noise prediction using PIV datasets. AIAA Paper 2004-2978; 2004.
[20] Papp JL. Calibration and validation of EASM turbulence model for jet flowfields. AIAA Paper 2002-0855; 2002.
[21] Georgiadis NJ, Rumsey CL, Yoder DA, Zaman KBMQ. Turbulence modeling effects on calculation of lobed nozzle flowfields. J Propul Power 2006;22(3):567–75.
[22] Lighthill MJ. On sound generated aerodynamically, I. General theory. Proc R Soc London A 1952;211: 564–87.
[23] Lighthill MJ. On sound generated aerodynamically, II. Turbulence as a source of sound. Proc R Soc London A 1954;222:1–32.
[24] Khavaran A, Bridges J, Georgiadis N. Prediction of turbulence-generated noise in unheated jets, Part 1: JeNo technical manual. NASA TM 2005-213827; 2005.
[25] Shih SH, Hixon DR, Mankbadi RR, Pilon A, Lyrintzis A. Evaluation of far-field jet noise prediction methods. AIAA Paper 97-0282; 1997.
[26] Birch SF, Lyubimov DA, Secundov AN, Yakubovsky KY. Numerical modeling requirements for coaxial and chevron nozzle flows. AIAA Paper 2003-3287; 2003.
[27] Birch SF. A review of axisymmetric jet flow data for noise applications. AIAA Paper 2006-2602; 2006.
[28] Kenzakowski DC, Papp J, Dash SM. Evaluation of advanced turbulence models and variable Prandtl/Schmidt number methodology for propulsive flows. AIAA Paper 2000-0885; 2000.
[29] Kenzakowski DC. RANS modeling improvements for jets using scalar variance equations. AIAA Paper 2006-0491; 2006.
[30] Koch LD, Bridges JE, Khavaran A. Flowfield comparisons from three Navier–Stokes solvers for an axisymmetric separate flow jet. AIAA Paper 2002-0672; 2002.
[31] Engblom WA, Khavaran A, Bridges JE. Numerical prediction of chevron nozzle noise reduction using Wind-MGBK methodology. AIAA Paper 2004-2979; 2004.
[32] Abdol-Hamid KS, Pao SP, Hunter CA, Deere KA, Massey SJ, Elmiligui A. PAB3D: Its history in the use of turbulence models in the simulation of jet and nozzle flows. AIAA Paper 2006-489; 2006.
[33] Pao SP, Abdol-Hamid KS, Campbell RL, Hunter CA, Massey SJ, Elmiligui A. Unstructured CFD and noise prediction methods for propulsion airframe aeroacoustics. AIAA Paper 2006-2597; 2006.
[34] Thies AT, Tam CKW. Computation of turbulent axisymmetric and nonaxisymmetric jet flows using the k–ε model. AIAA J 1996;34(2):309–16.
[35] Sarkar S, Erlebacher G, Hussaini MY, Kreiss HO. The analysis and modeling of dilatational terms in compressible turbulence. J Fluid Mech 1991;227:473–93.
[36] Sarkar S, Lakshmanan B. Application of a Reynolds stress turbulence model to the compressible shear layer. AIAA J 1991;29(5):743–9.
[37] Pope SB. An explanation of the turbulent round-jet/plane-jet anomaly. AIAA J 1978;16(3):279–81.
[38] Tam CKW, Ganesan A. Modified k–ε turbulence model for calculating hot jet mean flows and noise. AIAA J 2004;42(1):26–34.
[39] Abdol-Hamid KS, Pao SP, Massey SJ, Elmiligui A. Temperature corrected turbulence model for high temperature jet flow. J Fluids Eng 2004;126(5):844–50.
[40] Massey SJ, Thomas RH, Abdol-Hamid KS, Elmiligui AA. Computational and experimental flow field analyses of separate flow chevron nozzles and pylon interaction. AIAA Paper 2003–3212; 2003.
[41] Engblom WA, Georgiadis NJ, Khavaran A. Investigation of a variable-diffusion turbulence model correction for round jets. AIAA Paper 2005-3085; 2005.
[42] Georgiadis NJ, Yoder DA, DeBonis JR. A comparison of three Navier–Stokes solvers for exhaust nozzle flowfields. AIAA Paper 99-0748; 1999.
[43] Chien K-Y. Predictions of channel and boundary layer flows with a low-Reynolds-number turbulence model. AIAA J 1982;20(1):33–8.
[44] Menter FR. Zonal two equation k–ω turbulence models for aerodynamic flows. AIAA Paper 93-2906; 1993.
[45] Menter FR. Two-equation eddy-viscosity turbulence models for engineering applications. AIAA J 1994;32(8): 1598–605.
[46] Jones WP, Launder BE. The prediction of laminarization with a two-equation model of turbulence. Int J Heat Mass Transfer 1972;15:301–14.
[47] Dembowski MA, Georgiadis NJ. An evaluation of parameters influencing jet mixing using the WIND Navier–Stokes code. NASA TM 2002-211727; 2002.
[48] Franko KJ, Georgiadis NJ. Computational investigation of heated high-speed coaxial jets. AIAA Paper 2004-2980; 2004.
[49] Wilcox DC. Reassessment of the scale-determining equation for advanced turbulence models. AIAA J 1988;26(11): 1299–310.
[50] Dalbello T, Georgiadis NJ, Yoder DA, Keith TG. Computational study of axisymmetric off-design nozzle flows. AIAA Paper 2004-0530; 2004.

[51] Menter FR, Rumsey CL. Assessment of two-equation turbulence models for transonic flows. AIAA Paper 94-2343; 1994.
[52] Bridges JE, Wernet MP. Measurements of the aeroacoustic sound source in hot jets. AIAA Paper 2003-3130; 2003.
[53] Zaman KBMQ, Wang FY, Georgiadis NJ. Noise, turbulence, and thrust of subsonic free jets from lobed nozzles. AIAA J 2003;41(3):398–407.
[54] Seiner JM, Ponton MK, Jansen BJ, Lagen NT. The effect of temperature on jet noise emission. AIAA Paper 92-02-046; 1992.
[55] Barber TJ, Chiappetta LM, DeBonis JR, Georgiadis NJ, Yoder DA. An assessment of parameters influencing the prediction of shear layer mixing. J Propul Power 1999;15(1):45–53.
[56] Ayyalasomayajoula H, Kenzakowski DC, Papp JL, Dash SM. Assessment of k–ε/EASM turbulence model upgrades for analyzing high speed aeropropulsive flows. AIAA Paper 2005-1101; 2005.
[57] Yoder DA. Initial evaluation of an algebraic Reynolds stress model for compressible turbulent shear flows. AIAA Paper 2003-0548; 2003.
[58] Nelson CC, Power GD. CHSSI Project CFD-7: the NPARC alliance flow simulation system. AIAA Paper 2001-0594; 2001.
[59] Krist SL, Bierdon RT, Rumsey CL. CFL3D user's manual (version 5.0). NASA TM 1998-208444; 1998.
[60] Spalart PR, Allmaras SR. A one-equation turbulence model for aerodynamic flows. La Rech Aerosp 1994;(1): 5–21.
[61] Spalart PR, Allmaras SR. A one-equation turbulence model for aerodynamic flows. AIAA Paper 92-0439; 1992.
[62] Rumsey CL, Gatski TB, Morrison JH. Turbulence model predictions of strongly curved flow in a U-duct. AIAA J 2000;38(8):1394–402.
[63] Rumsey CL, Gatski TB. Recent turbulence model advances applied to multielement airfoil computations. J Aircr 2001; 38(5):904–10.
[64] Rumsey CL, Gatski TB. Summary of EASM turbulence models in CFL3D with validation test cases. NASA TM 2003-212431; 2003.
[65] Georgiadis NJ, Chitsomboon T, Zhu J. Modification of the two-equation turbulence model in NPARC to a Chien low Reynolds number k–ε formulation. NASA TM 106710; 1994.
[66] Khavaran A. Role of anisotropy in turbulent mixing noise. AIAA J 1999;37(7):832–41.
[67] Georgiadis NJ, Papamoschou D. Computational investigations of high-speed dual-stream jets. AIAA Paper 2003-3311; 2003.
[68] Georgiadis NJ, Papamoschou D. Computations of dual-stream jets with eccentric and coaxial bypass streams. AIAA Paper 2004-2981; 2004.
[69] Freund JB, Moin P. Mixing enhancement in jet exhaust using fluidic actuators: direct numerical simulations. In: FEDSM 98-5235, ASME, Proceedings of FEDSM'98, 1998.
[70] Freund JB, Lele SK, Moin P. Direct simulation of a Mach 1.92 jet and its sound field. AIAA/CEAS Paper 98-2291; 1998.
[71] Freund JB. Direct numerical simulation of the noise from a Mach 0.9 jet. In: FEDSM 99-7251, ASME, Proceedings of FEDSM'99, 1999.
[72] Nelson CC. Simulations of spatially evolving compressible turbulence using a local dynamic subgrid model. PhD thesis, Georgia Institute of Technology; 1997.
[73] Smagorinsky J. General circulation experiments with the primitive equations, part I: the basic experiment. Mon Weather Rev 1963;91:99–152.
[74] Moin P, Squires K, Cabot W, Lee S. A dynamic subgrid-scale model for compressible turbulence and scalar transport. Phys Fluids A 1991;3(11):2746–57.
[75] Rogallo RS, Moin P. Numerical simulation of turbulent flows. Annu Rev Fluid Mech 1984;16:99–137.
[76] Ragab SA, Sheen SC. Large eddy simulation of complex engineering and geophysical flows. Large eddy simulation of mixing layers, 1st ed. Cambridge: Cambridge University Press; 1993. p. 255–85.
[77] Choi D, Barber TJ, Chiapetta LM, Nishimura M. Large eddy simulation of high-Reynolds number jet flows. AIAA Paper 99-0230; 1999.
[78] Bodony DJ, Lele SK. On using large-eddy simulation for the prediction of noise from cold and heated turbulent jets. Phys Fluids 2005;17(085103):1–20.
[79] Constantinescu GS, Lele SK. Large Eddy simulation of a near sonic turbulent jet and its radiated noise. AIAA Paper 2001-0376; 2001.
[80] Boersma BJ, Lele SK. Large Eddy simulation of a Mach 0.9 turbulent jet. AIAA Paper 99-1874; 1999.
[81] Lele SK. Compact finite difference schemes with spectral-like resolution. J Comput Phys 1992;103:16–42.
[82] Bogey C, Bailly C. Computation of a high Reynolds number jet and its radiated noise using large eddy simulation based on explicit filtering. Comput Fluids 2006; 35(10):1344–58.
[83] Bailly C, Bogey C. Contributions of computational aeroacoustics to jet noise research and prediction. Int J Comput Fluid Dyn 2004;18(6):481–91.
[84] Bogey C, Bailly C, Juve D. Noise investigation of a high subsonic moderate reynolds number jet using a compressible LES. Theor Comput Fluid Dyn 2003;16:273–97.
[85] Tam CKW, Webb JC. Dispersion relation-preserving finite difference schemes for computational aeroacoustics. J Comput Phys 1993;107:262–81.
[86] Shur ML, Spalart PR, Strelets MK. Noise prediction for increasingly complex jets Part I: methods and tests. Int J Aeroacoust 2005;4(3&4):213–46.
[87] Shur ML, Spalart PR, Strelets MK. Noise prediction for increasingly complex jets: Part II: applications. Int J Aeroacoust 2005;4(3&4):247–66.
[88] Bodony DJ, Lele SK. Review of the current status of jet noise predictions using large-eddy simulations. AIAA Paper 2006-0468; 2006.
[89] Andersson N, Eriksson L-E, Davidson L. A study of Mach 0.75 jets and their radiated sound using large-eddy simulation. AIAA Paper 2004-3024; 2004.
[90] Bogey C, Bailly C. LES of a high Reynolds, high subsonic jet: effects of the subgrid modellings on flow and noise. AIAA Paper 2003-3557; 2003.
[91] Zhao W, Frankel SH, Mongeau L. Large eddy simulations of sound radiation from subsonic turbulent jets. AIAA J 2001;39(8):1469–77.

[92] DeBonis JR, Scott JN. A large-eddy simulation of a turbulent compressible round jet. AIAA J 2002;40(5): 1346–54.
[93] DeBonis JR. A large-eddy simulation of a high reynolds number Mach 0.9 jet. AIAA Paper 2004-3025; 2004.
[94] Paliath U, Morris P. Prediction of noise from jets with different nozzle geometries. AIAA Paper 2004-3026; 2004.
[95] Bogey C, Bailly C. A family of low dispersive and low dissipative explicit schemes for flow and noise computations. J Comput Phys 2004;194:194–214.
[96] Hixon R. A new class of compact schemes. AIAA Paper 98-0367; 1998.
[97] Gaitonde DV, Visbal MR. Further development of a Navier–Stokes solution procedure based on higher-order formulas. AIAA Paper 99-0557; 1999.
[98] Durran DR. Numerical methods for wave equations in geophysical fluid dynamics. Berlin: Springer; 1999.
[99] Visbal MR, Gaitonde DV. High-order accurate methods for unsteady vortical flows on curvilinear meshes. AIAA Paper 98-0131; 1998.
[100] Hixon R. Prefactored compact filters for computational aeroacoustics. AIAA Paper 99-0358; 1999.
[101] C.A. Kennedy, M.H. Carpenter, Comparison of several numerical methods for simulation of compressible shear layers. NASA TP 3484; 1997.
[102] Vasilyev OV, Lund TS, Moin P. A general class of commutative filters for LES in complex geometries. J Comput Phys 1998;146:82–104.
[103] Al-Qadi I, Scott JN. Simulations of unsteady behavior in under-expanded supersonic rectangular jets. AIAA Paper 2001-2119; 2001.
[104] Visbal MR, Gaitonde DV. Shock capturing using compact-differencing based methods. AIAA Paper 2005-1265; 2005.
[105] Roe PL. Characteristic-based schemes for the Euler equations. Ann Rev Fluid Mech 1986;18:337–65.
[106] Fureby C, Grinstein FF. Monotonically integrated large eddy simulation of free shear flows. AIAA J 1999;37(5): 544–56.
[107] Grinstein FF, Fureby C. Recent progress on MILES for high Reynolds number flows. J Fluids Eng 2002;124: 848–61.
[108] DeBonis JR, Scott JN. Truncation error characteristics of numerical schemes for computational aeroacoustics, AIAA Paper 2001-1098; 2001.
[109] Jameson A, Schmidt W, Turkel E. Numerical solutions of the Euler equations by finite volume methods using Runge–Kutta time-stepping schemes. AIAA Paper 81-1259; 1981.
[110] Stanescu D, Habashi WG. 2N-storage low dissipation and dispersion Runge–Kutta schemes for computational acoustics. J Comput Phys 1998;143(12):674–81.
[111] Hu FQ, Hussaini MY, Manthey JL. Low-dissipation and low-dispersion Runge–Kutta schemes for computational acoustics. J Comput Phys 1996;124:177–91.
[112] Carpenter MH, Kennedy CA. Fourth-order 2N-storage Runge–Kutta schemes. NASA TM 109112; 1994.
[113] Bogey C, Bailly C. LES of a high Reynolds, high subsonic jet: effects of the inflow conditions on flow and noise. AIAA Paper 2003-3170; 2003.
[114] Glaze DJ, Frankel SH. Stochastic inlet conditions for large-eddy simulation of a fully turbulent jet. AIAA J 2003; 41(6):1064–73.
[115] Yoder DA, Georgiadis NJ, Wolter JD. Quadrant CFD analysis of a mixer-ejector nozzle for HSCT applications. NASA TM 2005-213602; 2005.
[116] Thomas RH, Kinzie KW. Jet–pylon interaction of high bypass ratio separate flow nozzle configurations. AIAA Paper 2004-2827; 2004.
[117] Mahesh K, Constantinescu G, Moin P. A numerical method for large-eddy simulation in complex geometries. J Comput Phys 2004;197:215–40.
[118] Liu Y, Vinokur M. Multi-dimensional spectral difference method for unstructured grids. AIAA Paper 2005-0320; 2005.
[119] Hesthaven JS, Warburton T. High-order unstructured grid methods for time-domain electromagnetics. AIAA Paper 2002-1092; 2002.
[120] Pope S. Ten questions concerning the large-eddy simulation of turbulent flows. New J Phys 2004;6(35).
[121] Rowley CW, Colonius T. Discretely nonreflecting boundary conditions for linear hyperbolic systems. J Comput Phys 2000;157:500–38.
[122] Colonius T, Lele SK, Moin P. Boundary conditions for direct computation of aerodynamic sound generation. AIAA J 1993;31(9):1574–82.
[123] Poinsot TJ, Lele SK. Boundary conditions for direct simulation of compressible viscous flows. J Comput Phys 1992;101:104–29.
[124] Giles MB. Nonreflecting boundary conditions for Euler equation calculations. AIAA J 1990;28(12):2050–8.
[125] Freund JB. Proposed inflow/outflow boundary condition for direct computation of aerodynamic sound. AIAA J 1997;35(4):740–2.
[126] Batten P, Goldberg U, Chakravarthy S. Interfacing statistical turbulence closures with large-eddy simulation. AIAA J 2004;42(3):485–92.
[127] Arunajatesan S, Kannepalli C, Dash SM. Progress towards hybrid RANS-LES modeling for high-speed jet flows. AIAA Paper 2002-0428; 2002.
[128] Urbin G, Knight D. Compressible large eddy simulation using unstructured grid: supersonic turbulent boundary layer and compression corner. AIAA Paper 99-0427; 1999.
[129] Piomelli U. Large-eddy simulation: achievements and challenges. Prog Aerosp Sci 1999;35:335–62.
[130] Bogey C, Bailly C. Decrease of the effective Reynolds number with eddy-viscosity subgrid-scale modeling. AIAA J 2005;43(2):437–9.
[131] Ghosal S, Moin P. The basic equations for the large-eddy simulation of turbulent flows in complex geometry. J Comput Phys 1995;118(1):24–37.
[132] Thurow BS, Blohm M, Lempert WR, Samimy M. High repetition rate planar velocity measurements in a Mach 2.0 compressible axisymmetric jet. AIAA Paper 2005-0515; 2005.
[133] Panda J, Seasholtz RG. Experimental investigation of the differences between Reynolds averaged and Favre averaged velocity in supersonic jets. AIAA Paper 2005-0514; 2005.
[134] Panda J, Zaman KBMQ. Measurement of initial conditions at nozzle exit of high speed jets. AIAA Paper 2001-2143; 2001.